Full title: Identifying optimal working points of individual Virtual Brains: A large-scale brain network modelling study

Short title: Optimal working points of individual Virtual Brains

Paul Triebkorn*[1,2], Joelle Zimmermann[3], Leon Stefanovski[1,2,] Dipanjan Roy[4], Ana Solodkin[5], Viktor Jirsa[6], Gustavo Deco[7], Michael Breakspear[8], Anthony Randal McIntosh[3,] Petra Ritter*[1,2]

1. Brain Simulation Section, Department of Neurology, Charité Universitätsmedizin and Berlin Institute of Health, Berlin, Germany
2. Bernstein Center for Computational Neuroscience, Berlin, Germany
3. Baycrest Health Sciences, Rotman Research Institute, Toronto, Canada
4. National Brain Research Centre, Manesar, India
5. Anatomy & Neurobiology and Neurology, UC Irvine Health, Irvine, USA
6. Institut de Neurosciences des Systèmes, Aix Marseille Université, Marseille, France
7. Center for Brain and Cognition, Department of Information and Communication Technologies, Universitat Pompeu Fabra, Barcelona, Spain
8. QIMR Berghofer Medical Research Institute, Herston, Australia

* Corresponding authors

E-mail: jan-paul.triebkorn@charite.de; petra.ritter@charite.de

Abstract

Using The Virtual Brain (TVB, thevirtualbrian.org) simulation platform, we explored for 50 individual adult human brains (ages 18-80), how personalized connectome based brain network modelling captures various empirical observations as measured by functional magnetic resonance imaging (fMRI) and electroencephalography (EEG). We compare simulated activity based on individual structural connectomes (SC) inferred from diffusion weighted imaging with fMRI and EEG in the resting state. We systematically explore the role of the following model parameters: conduction velocity, global coupling and graph theoretical features of individual SC. First, a subspace of the parameter space is identified for each subject that results in realistic brain activity, i.e. reproducing the following prominent features of empirical EEG-fMRI activity: topology of resting-state fMRI functional connectivity (FC), functional connectivity dynamics (FCD), electrophysiological oscillations in the delta (3-4 Hz) and alpha (8-12 Hz) frequency range and their bimodality, i.e. low and high energy modes. Interestingly, FCD fit, bimodality and static FC fit are highly correlated. They all show their optimum in the same range of global coupling. In other words, only when our local model is in a bistable regime we are able to generate switching of modes in our global network. Second, our simulations reveal the explicit network mechanisms that lead to electrophysiological oscillations, their bimodal behaviour and inter-regional differences. Third, we discuss biological interpretability of the Stefanescu-Jirsa-Hindmarsh-Rose-3D model when embedded inside the large-scale brain network and mechanisms underlying the emergence of bimodality of the neural signal.

With the present study, we set the cornerstone for a systematic catalogue of spatiotemporal brain activity regimes generated with the connectome-based brain simulation platform The Virtual Brain.

Author Summary

In order to understand brain dynamics we use numerical simulations of brain network models. Combining the structural backbone of the brain, that is the white matter fibres connecting distinct regions in the grey matter, with dynamical systems describing the activity of neural populations we are able to simulate brain function on a large scale. In order to make accurate prediction with this network, it is crucial to determine optimal model parameters. We here use an explorative approach to adjust model parameters to individual brain activity, showing that subjects have their own optimal point in the parameter space, depending on their brain structure and function. At the same time, we investigate the relation between bistable phenomena on the scale of neural populations and the changed in functional connectivity on the brain network scale. Our results are important for future modelling approaches trying to make accurate predictions of brain function.

Introduction

Brain network models allow us to investigate how realistic neural behaviour arises as a function of variations in specific neural parameters. Large-scale brain network models combine empirical data from multiple modalities into a framework where we can test predictions using non-invasive techniques in humans (1). These models take as input imaging data, for instance the structural connectivity (SC) map of white matter pathways derived from diffusion weighted imaging, and predict brain behaviour. Models are used to estimate how this behaviour arises as a function of the anatomical connectome taking into account features such as noise (stochastic fluctuations in the signal due to internal and external factors), transmission delays (the speed with which the signal travels along physical pathways), or connectivity weighting (the strength of pathways between regions). Realistic values of these features in the brain are then estimated by fitting the simulated signal to the empirical signal.

The Virtual Brain

The Virtual Brain (TVB; thevirtualbrain.org) is a simulation platform that integrates local neural mass models with large-scale long-range global connectivity dynamics driven by individual SC(2–7). A unique feature of TVB is the ability to model "personalized virtual brains", whereby an individual's DTI derived SC, optionally combined with directionality information from CoCoMac, constrains the inter-regional interactions. This allows researchers to make subject-specific hypotheses, and to investigate individual differences in parameter values (i.e. of conduction speed, etc.) that may lead to biologically significant neural activity. TVB has previously been used, for example, to model biophysical correlates of recovery after stroke in adults(8,9), and children(10),, or brain activity dynamics pre and post surgery in brain tumor patients(11,12) with the goal of aiding the design of therapeutic interventions(13), or to identify biophysical mechanisms underlying seizure dynamics, with the ability to accurately predict spatial spread of the epileptic seizure (14,15). With the healthy connectome, TVB has been used for instance to study the timing of cognition neural behaviour during transcranial direct current stimulation (16), effects of plasticity and learning(17) or to understand individual structure-function relations in healthy individuals(18).
(See http://www.thevirtualbrain.org/tvb/zwei/neuroscience-publications for a full list of publications).

The TVB model combines local (at the level of neural populations) and global (network-level) features to capture the dynamics of the neural system. A local model, for example the Stefanescu-Jirsa Hindmarsh-Rose 3D (SJHMR3D)(19) defines the mean-field behaviour at the nodal level (see below for a detailed description). Local dynamics are then

integrated across the system via the long-range fibers represented by the individual's SC and global parameters such as conduction speed and long-range coupling, which describe the structural-temporal integration across the cortex. Optimal model fit (simulated FC to empirical FC) is highly dependent on the global coupling and conduction speed values. (8,9,13,18,20–23)**.** See equation 1 in Methods for a mathematical description of these parameters.

Conduction Velocity: Conduction velocity describes the speed with which the signal travels between the nodes, and is used to estimate time delays based on distances derived from an individual's diffusion tractography. Thus, propagation of neural signal will be faster for dense, myelinated neural fibers compared to smaller fibers for the same distance (24). With a fixed distance, a large conduction velocity will result in a short time delay; a small conduction velocity will result in a large time delay and slower system. Conduction velocity in TVB and similar models has been associated with important features of healthy and diseased brains (9,21,22).

Global coupling: Long-range global coupling describes the balance of local and global dynamics, and consequently has an effect on the resulting efficiency of the system(8). The long-range coupling is a scaling factor for the individual's tractography-derived connectivity weights. Higher long-range global coupling describes a system where the local (intra-regional) dynamics have a stronger influence on a region's activity compared to the global (inter-regional) dynamics. That is, the inputs from within the regions play a stronger role than the input from other regions. Conversely, a low global coupling means that global dynamics have a stronger influence compared to local dynamics. Long-range coupling parameter values in TVB may serve as relevant biomarkers to identify clinical populations (8). Specifically, long-range global coupling in TVB has been associated with important neural mechanisms in health as well as disease. For example: tuning the network close to a bifurcation point (25), exploration of the dynamical landscape (21)**,** motor recovery in stroke (8–10), seizure activity (26), Alzheimer's disease (27–29) efficiency of the system in the pathological brain(8). Moreover, alpha band power in an MEG model was a function of transmission delays and global cortical coupling(30). Optimal global parameters have been shown to give rise to a number of empirical resting-state behaviours such as network synchronization(31), fluctuations in the stability of the system leading to the emergence of new resting-state networks (RSN)(25), changes in the attractor landscape(32), the engagement and disengagement of various subnetworks (33), and realistic alpha band activity(30). An optimal point in these parameters defines the manifestation of these behaviours.

Previous TVB Studies

Several studies with TVB are limited by the number of metrics fitted (often a single metric such as FC fit), modalities simulated, sample size, and/or are focused on pathological changes in these neural parameters lacking a full

investigation of the healthy brain. The following are a few examples. We are focusing here on what our present study provides beyond state-of the art. Thereby we acknowledge the value of these previous publications on which our present study builds to further extend our present scope of understanding Falcon et al (2015, 2016) investigated stroke in TVB have a sample size of 30 (31) subjects. These authors explored global coupling, conduction velocity, and local coupling (K12, K11 and K21) of the SJHMR3D model (8,9). The simulated data was validated by comparing to empirical in terms of amplitude, frequency and FC. The parameters were optimized in a stepwise manner, rather than exploring the full grid of all parameter combinations as done in the present study. Another study on exclusively healthy subjects used the same local model and the SC of 9 individuals to fit simulated FCs to their empirical counterpart (18). This procedure was also used in another study when varying global coupling to simulate 42 virtual brains (10). In the study of Kunze et al., the standard SC provided by TVB was used to assess the effect of transcranial direct current stimulation (tDCS) on frequency, FC and postsynaptic potentials of pyramidal cells (16). These authors varied the parameters global coupling and maximum voltage scaling of the tDCS. In another study, the effect of different parcellation size and short-range connectivity on simulation results was investigated using 10 random connectomes of the human connectome project (14). Different number of regions, global and local coupling parameters and different local models (Reduced Wong-Wang and FitzHugh-Nagumo) were simulated and later analysed with graphtheoretical measures, entropy and principal component analysis. A Hopf-Bifurcation model was used in the study of Deco et al. fitting simulated blood oxygenation level dependent (BOLD) signal to empirical FC and FCD (34). The optimal fit was found tuning a local bifurcation parameter and global coupling. Tuning of a single excitability parameter of the Epileptor model was used to model individual epileptic brains for 1 and 15 patients, respectively (14,15). The simulated data was fitted to determine clinical epilepsy propagation zones. TVB was also used to simulate rat brains (35) and macaque brains(36). With an evolutionary optimization algorithm and the Generic 2D oscillator the simulated FC was tuned to fit its empirical counterpart.

In sum, parameter grid-search explorations and FC fitting are a common approach in brain modelling. In the present study, we utilize a larger sample size (N = 50) of healthy subjects across the full age spectrum, and a more detailed description of the effects from parameters on neural and BOLD signal, as well as the convergence across several fitting metrics.

Present Study

We conduct a comprehensive parameter exploration of personalized brain network models in a sample of 50 healthy

human brains (18 to 80 years of age, mean 41.12 ± 18.20; 30 females and 20 males) using TVB. The goal is to show that there exists a specific set of neural parameters for which virtual brains operate in a biologically realistic manner in the resting-state, and that these parameters converge at a particular, unique, point for each individual across several metrics. Typically, a single correlation metric for comparison of FCs, for a single modality, is used to assess model fit in simulations studies. Yet, the assessment across multiple modalities and metrics is critical in order to validate how optimal models are.

We show that there exists a particular subset in the parameter space, unique to each individual, where several metrics converge to produce the best fit of the simulated to the empirical data, and reproduce important empirical features of EEG and fMRI. The results are shown for alpha as well as delta frequency electrophysiological activity. Specifically, we show that this optimal fit parameter subset is similar for the following metrics: 1) the correlation between empirical and simulated BOLD FC, 2) fit of simulated to the empirical BOLD FCD 3) frequency of the mean neural signal, as well as 4) a bimodal power distribution of the neural signal at an alpha frequency, a feature that has been observed in empirical(37–41), and simulated (42,43) EEG data(44,45). Our simulations reveal the mechanisms that lead to the bimodal behaviour, as well as inter-regional differences in bimodality.

High-power alpha-frequency oscillations are a robust finding in resting-state electroencephalography (EEG) of the human brain(39–41,44,46–48). Bimodality in the distribution of the power in the alpha frequency band refers to the bursting between two distinct modes that is observed in the empirical signal (37,38)and has also been modelled as a function of noise(42). The characterization of the power distribution provides more information about the temporal behaviour of the system than the traditional power spectrum, which reports only the mean power. The bimodality that is observed in the empirical signal demarcates a switching, or bimodality, between low and high amplitude alpha oscillations arising from a dynamical instability of the system in the presence of stochastic noise (37,38,42). In recent work, TVB simulations have demonstrated feasibility to simulate alpha oscillations (17,18). To date its capability to reproduce bimodality of alpha has not been explored.

We here investigate how empirical-simulated fMRI FC correlations and the electrophysiological alpha frequency power distribution vary as a function of conduction velocity and long-range coupling. We focus on the global parameters of conduction velocity and long-range coupling because these variables have an influence on the large-scale spatiotemporal dynamics. In addition, we will also report the effect of local inhibitory and excitatory synaptic coupling

parameters (parameters K12 = inhibitory on excitatory, K11 = recurrent excitatory, K21 = excitatory on inhibitory) (19) within a single (i.e. unconnected) population model.

Methods

Data acquisition

Simultaneous EEG-fMRI data, dwMRI, and structural MRI were recorded from 50 healthy adult subjects at Berlin Center for Advanced Imaging, Charité University Medicine, Berlin, Germany (18 to 80 years of age, mean 41.12 ± 18.20; 30 females and 20 males). Subjects were voluntarily recruited, and had no self-reported history of cognitive, neurological or psychiatric conditions. Informed consent was provided to subjects before participating in the study, and the research was conducted in accordance with the Code of Ethics of the World Medical Association Declaration of Helsinki, and approved by the local ethics community at Charité University. The data acquisition procedures are those reported by our colleagues (18)and are summarized here.

Images were acquired on a Siemens Tim Trio MR scanner (12-channel Siemens head coil). Anatomical and dwMRI acquisition was performed first, after which subjects were taken out of the scanner to have their EEG cap set up. Subjects then returned to the scanner for simultaneous EEG-fMRI measurements. Subjects lay in the scanner with their eyes closed and were asked not to fall asleep.

High resolution 1×1×1mm T1-weighted scans were acquired with an MPRAGE sequence: repetition time (TR) = 1900ms, echo time (TE) = 2.25ms, flip angle (FA) = 98, field of view (FoV) = 256mm, 256 matrix, 192 sagittal slices, slice thickness = 1mm. EEG and fMRI were recorded for 22 minutes at resting state. We used an echo planar imaging (EPI) T2* sequence: 666 volumes, TR = 1940 ms, TE = 30ms, FA = 788, FoV = 192, 64 matrix, voxel size = 3×3×3 mm^3, 32 transversal slices, slice thickness = 3mm. The first five images of the blood oxygen level dependent (BOLD) fMRI series were removed to prevent disturbance from saturation effects. Diffusion-weighted MR echo-planar measurements were conducted with: TR = 7500ms, TE = 86ms, FoV = 220mm, 96 matrix, voxel size = 2.3×2.3×2.3mm, 61 transversal slices, slice thickness = 2mm; 64 diffusion gradient directions with b-values = 1000 s/mm^2.

Brain imaging data preprocessing

Preprocessing of anatomical, diffusion and functional data was performed using our pipeline for derivation of individual connectomes (49). The preprocessing steps are described in detail there, and more briefly below. Preprocessing of T1-weighted images included the following: motion correction, intensity normalization, extraction of non-brain tissue, brain mask generation, and segmentation of cortical and subcortical grey matter. We used the parcellation from the Desikan-Killiany Atlas (50) implemented in FREESURFER to divide the cortex into 68 regions of interest. A quality check of the parcellation of individual high-resolution T1-weighted scans was performed manually.

The dwMRI data was preprocessed as follows: motion and eddy current correction, linear registration of b0 image to

individual T1-weighted image. The anatomical cortical parcellations were transformed to individual diffusion space, where probabilistic tractography was conducted. Spherical deconvolution was applied to constrain tractography, using MRTrix streaming method, which has the ability to identify crossing fibers (FA threshold = 0.1)(51). The gray matter – white matter interface was exhaustively sampled, streamlining up to 200,000 times from each voxel (radius of curvature = 1mm, maximum length = 300mm). Binary connections for each region pair, based on the Desikan-Killiany atlas, were then aggregated, and a 68 by 68 SC was obtained. The region labels are listed in Table S1. A weights and distance matrix was calculated for each subject. Weights matrices were the number of voxel pairs between two ROIs with at least one track found. We modified the weights matrix by using the common logarithm of its values and then normalizing to its highest value. Distance matrices were the mean track length of fibers between each pair of ROIs, measured in mm.

In brief, the functional data was preprocessed as follows: motion correction, brain extraction, high-pass filter (100s), registration to individual T1-weighted anatomical scans to apply high-resolution parcellation mask to the fMRI. Additionally, quality of BOLD signal was analyzed with temporal signal to noise to maps (52).. BOLD signal was averaged across voxels within brain regions. Functional connectivities were computed using a Pearson's linear correlation coefficient on the BOLD data of each region pair.

The TVB Model: Local and Global Dynamics

Global Dynamics

The global behaviour of the system is driven by interactions between individual nodes, as described by the conduction velocity and long-range coupling.

The local dynamics at a node i can be described by **Eq. 1**

$$x_i(t+1) = x_i(t) + f\left(x_i(t)\right)dt + c\sum_{j=1}^{N} w_{ij}\, x_j\left(t-\Delta t_{ij}\right)dt + \sqrt{2*D} + \sqrt{dt} + \eta(t) \qquad 1$$

Eq. 1 Global equation of TVB

The local mean-field potential of node i is integrated across time t=1:T by taking the sum of its current potential $x_i(t)$, the derivative of the local model $f(x_i(t))dt$, the scaled input of all other nodes j=1:N and the influence of noise. The parameter D scales the dispersion of the gaussian distribution from which random values are drawn $\eta(t)$. Connectivity weights (i.e. individual diffusion tractography derived structural connectivity weights combined with optional CoCoMac directionality information(53)) are defined here as w_{ij}, where the connection weight scales the influence of node j on node i. The time delays of signal propagation, $\Delta t_{ij} = d_{ij}/v$ are influenced by distances, d_{ij} (ie diffusion

tractography derived distances between regions), and conduction velocity, v. The long-range coupling factor, c, does an additional scaling of influence (15).

Simulations and global parameters

The simulations were performed with TVB v1.5. TVB input was the individual SC, and a combination of local and global parameters describing the nodal and network level dynamics. Different parameter combinations were simulated in two sets for each individual subject, with global and local parameters described in Table 1 and 2 respectively. The neural signal in the first set of simulation oscillated with a frequency of around 2-5 Hz whereas in the second set around 8-12Hz. We will call them delta and alpha sets respectively. All computations described in the following section were performed on a high performance computer consisting of multicore CPUs at a clock rate of ~2.50GHz per CPU core and 8GB RAM per core. The time per simulation was approximately 10h (1.6h) for integration step size 0.01220703125 ms (0.05ms) for the delta (alpha) set. In total we tested 1615 parameter combinations for each subject resulting in 80750 simulations with a total simulation length of ~ 6554h. The total computation time was ~230000h.

Table 1: Global parameters for delta and alpha sets.

Parameters	**Delta set**	**Alpha set**
Global coupling	linear	linear
a (multiplicative)	[0.05:0.01:0.25]	[0.025:0.0001:0.04]
b (additive)	0	0
Conduction speed	[20:20:100]	[10:10:100]
Integrator Integration step size Additive noise	HeunStochastic dt = 0.01220703125 ms D = 1.0	HeunStochastic dt = 0.05 ms D = 0.001
Monitors: *SubSample* (of neural signal) sampling period BOLD HRF Kernel sampling period	 3.90625ms (= 256Hz) MixtureOfGammas 500ms (=2Hz)	 3.90625ms (= 256Hz) MixtureOfGammas 500ms (=2Hz)
Duration of simulated time series	180s	300s

Table 2: Local parameters in delta and alpha set simulations.

Parameter	**r**	**a**	**b**	**c**	**d**	**s**
Delta set	0,006	1.0	3.0	1.0	5.0	4.0
Alpha set	0,006	1.0	3.0	1.0	5.0	4.0
Parameter	**xo**	**K11**	**K12**	**K21**	**σ**	**μ**
Delta set	-1.6	0.5	0.1	0.15	0.3	2.2
Alpha set	-1.6	4.0	1.6	0.15	0.4	2.2

We coupled local nodes via long-range connections in the model. The anatomical connectome served as the structural backbone of these connections. In both sets, we varied two free parameters in order to examine the spatiotemporal dynamics: the global coupling which scales the input to a node from others and the conduction speed (mm/ms) which represented delays in the propagation of the signal. The global coupling scaling factor is named “a” in the TVB interface. In this article, we will refer to it as just global coupling or “G”. The goal was to achieve a good approximate fit between the simulated and empirical FCs. Due to changes of local parameters, we also changed the noise distribution and integration step size in the second set of simulations. BOLD time-series were generated by convolving the neural signal with a mixture of gamma kernel of 20s length (54).

Local Stefanescu-Jirsa 3D Model

We used a local Stefanescu-Jirsa 3D Hindmarsh-Rose (SJHMR3D) mean-field model (19) in TVB to simulate nodal neural behaviour. The SJHMR3D is a biologically realistic model based on a network of heterogeneous excitatory and inhibitory coupled Hindmarsh-Rose neurons (55) that exhibit a complex repertoire of neural behaviour - such as synchronization and random firing, multiclustering, bursting, transient oscillations and oscillation death. Coupled neurons of the detailed network showed reorganizing behaviour into clusters with similar dynamics. Using mode decomposition techniques the authors were able to capture cluster dynamics from the detailed network in a low dimensional representation of only 3 modes. The set of equations **Eq.2** describe local dynamics at a node *i, with each state variable being a vector of length 3 to represent the different modes.* SJHMR3D aims to describe the average membrane potential of a population of neurons that are electrically coupled. The model is comprised of six differential equations representing interconnected neural populations of excitatory (x, y, z), and inhibitory (w, v, u) populations as such:

$$
\begin{aligned}
\dot{x}_i &= y_i - a x_i^3 + b x_i^2 - z_i + \left[K_{11}\left(X_1 - x_i\right) - K_{12}\left(X_2 - x_i\right) \right] + IE_i \\
\dot{y}_i &= c_i - d x_i^2 - y_i \\
\dot{z}_i &= r s x_i - r z_i - m_i \\
\dot{w}_i &= v_i - a w_i^3 + b w_i^2 - u_i + K_{21}\left(X_1 - w_i\right) + II_i \\
\dot{v}_i &= h_i - p_i w_i^2 - v_i \\
\dot{u}_i &= r s w_i - r u_i - n_i
\end{aligned}
\qquad 2
$$

Eq. 2. Local dynamics of the SJHMR3D model.

Legend: x, y, z, v, w, u – state variables; a, b, c, d – constants representing fast ion channels; r – constant representing slow ion channels; s – bursting strength; IE, II – excitatory and inhibitory input current; K_{11} – excito-excitatory coupling; K_{12} – inhibito-excitatory coupling; K_{21} – excitato-inhibitory coupling; X_1, X_2 – mean field potential of inhibitory and excitatory subpopulation; m, n, p, h – constant parameters.

Here, *x(t) and w(t)* represents the membrane potential, *y(t) and v(t)* represents the recovery variable via fast ion channels, and *z(t) and u(t)* the inward current via slow channels in the membrane. From each simulation the state variables x and w have been recorded. Their three modes were averaged to generate the mean field potential of excitatory and inhibitory neurons. The local parameters that we used for the simulations are described in Table 2.

Our goal was to create resting state activity that shows the electrophysiological alpha band frequency oscillation that is present in empirical EEG data. In order to achieve faster oscillations in the alpha set we had to not only change the global but also the local parameters. Therefore, we conducted an exploration of the local model and its parameters which is described in detail in the supplementary materials S1 Text. Shortly summarized we simulated 2250 different combinations of parameters in an uncoupled network (i.e. connections weights = 0) to observe the effect of parameter changes on the local model. From there we selected those combinations which peaked around 8-12 Hz in the spectral density.

Data Analysis

All data preprocessing and analysis has been performed with Python and the statistical computing language R (56). Figs have been generated with the Python library Seaborn. In order to allow the neural signal to stabilize, and to account for random initial conditions in our simulation, we deleted the first 2 s of each simulated time series. The BOLD signal was simulated using a mixture of gammas kernel as a hemodynamic response function (HRF). To account for the 20 s length of the kernel, we removed the first 20s of the BOLD signal. For better comparison of simulated to empirical data, we down-sampled the simulated BOLD signal to a 2Hz sampling frequency. Simulated FC was derived by Pearson-correlating all brain regions' pairs of simulated BOLD signals. Correlation was also used to quantify similarities between the simulated and the empirical FC:

Bimodality: Hartigan's Dip Test

For every neural signal, we calculated a time-frequency analysis using Scipy's spectrogram function(57). The frequency with the highest power values in the spectrogram was then used to test for bimodality. We used Hartigan's Dip test (as implemented in R) on the distribution of power coefficients of the selected frequency to assess whether power is uni-modally or bi-modally distributed. With $p < 0.05$, we can reject our null-hypothesis that the distribution is unimodal and therefore it must at least be bimodal. Bimodality of the mean simulated neural signal was assessed, whereby mean neural signal was taken as the average of all regional time series. We also conducted this analysis on a regional level to account for potential regional differences in bimodality. For an example of unimodal and bimodal power distribution see Fig 1.

Fig 1. Example of a unimodal and a bimodal power distribution of the simulated neural signal of an individual subject. Time series in A and B were simulated using parameters as in the alpha set with different global coupling strength. G = 0.03 and G = 0.0328 for A and B respectively. Each panel depicts the neural signal, a time-frequency analysis and on the right the distribution of power coefficients at the highest power frequency for a unimodal (bimodal) signal. In B the time series and spectrogram show a switching between high and low amplitude oscillations. Hartigan's Dip Test p-values are 1 and <0.001 for the unimodal and bimodal distribution.

As the frequency of the oscillations varies across simulations, we are not assessing the same frequency for every simulation. Rather, we test the frequency that is most dominant in the signal, i.e. the frequency that has the highest power in spectrogram. Therefore subsequent figures which assess bimodality for a certain parameter range will have corresponding figures showing the dominant frequencies which were tested.

Functional Connectivity Dynamics (FCD)

It is known that FC is not static over time. It rather changes and switches between different modes during rest (58) but also during tasks(59), learning(60), sleep(61), sedation (62)and aging(63). Resting state FCD is also affected by diseases such as schizophrenia (64) or Alzheimer's (65)

The non-stationarity of functional connections has been modeled before already(66). Hansen et al. modeled a large-scale brain network model with three different local models. They show that only a mean field model with enhanced non-linearity was able to create switching between states in the FCD. Since our local model is highly non-linear we

expect to see dynamical changes in functional connections as well.

In order to characterize FCD, we required a longer simulation to be able to divide the time series into meaningful time windows. To this end, we conducted 22 minutes simulations for four sample subjects. We used local parameters and global coupling values from alpha set. Conduction speed was set to the subject specific optimum derived from the previous analysis of the alpha set simulations. For each simulated BOLD signal, we created an FCD matrix. Time windows of size 60s with an overlap of 40s were used for all FCDs. The fit between empirical and simulated FCD was assessed with Kolmogorov-Smirnoff Distance(34).

Subject Specificity

An important feature of TVB is to provide subject specific simulations. Since we know that structure shapes function (67–70) in the brain one could assume that by providing a subject specific input the output fits best to its own empirical data, i.e. by using individual SCs as a structural backbone of a simulation we generate data that is closer to its own empirical counterpart than to that when using SCs of other subjects. So far, we compared simulated to empirical FCs of the same subject to optimize our parameters. To test for subject specificity of our TVB model predictions, we compared all simulated FCs of a subject to the empirical FCs of all other subjects to determine whether the best fit is achieved with the subjects own FC or the FC of another subject.

Results

We conducted two sets of simulations and examined the effect of global parameters such as global coupling and conduction speed on the generated signal and the comparison to empirical data. In one set our chosen parameters produced delta-frequency activity (hence delta set), and in the other we modelled oscillations in the more prevalent alpha band frequency (hence alpha set), which is common in human EEG signal. Bimodality in this frequency range has been previously reported as a biological tenet of the signal (37,38,42). Because we were interested in the bimodality mechanisms in the alpha, we conducted more extensive exploration of the alpha set. Afterwards, we present the mechanism that generates bimodality in our model, and finally we focus on the subject specificity of our models.

Overview of the simulation sets.

In both simulation set the parameter conduction speed and global coupling were varied. In the first simulation set conduction speed was explored in a range from 20 mm/ms to 100 mm/ms in steps of 20 mm/ms and global coupling from 0.05 to 0.25 in steps of 0.01. This gave rise to 5250 simulations (50 subjects * 105 parameter combinations). For the second set, achieving bimodality in the alpha frequency oscillations, we varied conduction speed from 10 mm/ms to 100 mm/ms in steps of 10 mm/ms and global coupling from 0.025 to 0.04 in steps of 0.0001, for a total of 75500 simulations (50 subjects * 1510 parameter combination). Aside from different ranges for the global parameters, also the local parameters have changed (**Table 2**). All simulations were evaluated by their goodness of fit to their corresponding empirical FC by correlation. This produced one 3D matrix with the dimensions [subjects, conduction speed values, global coupling values] for each simulation set. The elements of the matrix are correlation coefficients. Similarly, a 3D matrix was calculated for bimodality and frequency analysis of the mean neural signal. To visualize our results we averaged over the [subjects] dimension of each 3D matrix. The result is a 2D matrix with dimensions [conduction speed and global coupling]. The elements are the averaged metrics. (**Fig 2**).

Fig 2. Overview of the parameter exploration generating oscillations in the alpha and delta rhythm range. Both sets varied the parameters conduction speed and global coupling, but across different ranges. 1st row shows prediction quality (comparison of simulated and empirical data) of all simulations averaged across all subjects. 2nd row bimodality assessed on the mean neural signal using Hartigan's dip test. 3rd row Frequency of the oscillating mean neural signal. For both simulation sets there is an overlap between best empirical-simulated FC fit and bimodality of the neural signal at distinct global coupling. 4th row Distribution of optimal parameter points for all subjects derived by correlation to empirical FC. Density plot is smoothed with a Gaussian kernel. Best fits can be seen across a wide range

of speed, but only few coupling values. The scatter plot showing a linear relation between optimal global coupling and average degree. (delta: r = -0.68, p < 0.0001, alpha r = -0.88, p < 0.1*10-15). Average degree was defined as the mean of row sums in each SC.

We demonstrate that best predictions of empirical signal features (FC, oscillations and bimodality of the neural signal) arise as a function of particular ranges of neural parameters, which we term the optimized parameters. Empirical features were optimally reproduced through our models at a wide range of conduction speeds, but only in a narrow range of global coupling values. For the delta (alpha) set these were around G = 0.1 – 0.14 (0.0280 – 0.031).

The mean best correlation to empirical data for individual subjects was 0.45 (0.514) with STD = 0.094 (0.088) and highest correlation = 0.66 (0.68) in the delta (alpha) set. The distribution of best correlations to empirical FCs are shown in **Fig 6** (**D**, red density estimate). We compared the alpha and delta sets, and found that correlation fits were in the same range (Wilcoxon signed-rank test on the distribution of best correlations of the two sets was non-significant). Bimodality can be seen at global coupling values between 0.11 and 0.14 (0.0286 – 0.031) and was more likely to appear at higher conduction speeds.(The fastest average oscillation was observed at lower couplings than the peaks of the two other metrics. As we increased global coupling from low absolute values, an increase in frequency was observed in the delta set. This continued until a critical point at which the oscillation speed began to decrease again. In the alpha set the frequency is continuously decreasing as a function of global coupling. However, if we explore the parameter space more to the left of the x-axis the same phenomenon, increasing frequency, should be visible. We will explain this mechanism later, when we explore bimodality.

Because averaging over subjects may obscure individual features of the signal, we also extracted an optimal parameter set for each subject. Optimal was defined as the best fit to empirical FC. The 50 resulting parameter combinations were plotted in a 2D density plot (**Fig 2 4th row**).

Again, we observed that best fits to empirical data were distributed across many conduction speed values but in a narrow range of global coupling. Interestingly, in the delta set there were two modes of highest fit along the conduction speed axis, suggesting a large degree of between-subject variability in this metric. Some subjects had best fits at conduction speeds around 40 mm/ms whereas others had best fits around 100 mm/ms. Within the alpha set the optimal parameters were distributed around one single mode. Distribution parameters of individual optimal points can be seen in

Table 3: Parameters of optimal working point distributions.

	Delta set		**Alpha set**	
	Global coupling	Conduction speed [mm/ms]	Global coupling	Conduction speed [mm/ms]
Median	0.14	80	0.03	50
Mean	0.1398	70.8	0.0304	50
Standard Dev.	0.0113	26.56	0,0021	25,0713

We found that the optimal global coupling is correlated to the average degree of the SC used for the simulation. In both simulation sets optimal coupling decreased with increasing average degree, $r = -0.68$, $p < 0.0001$ for delta and $r = -0.88$, $p < 0.1*10^{-15}$ for alpha set.

This is because the output of a node is multiplied by weights of the SC and then scaled by the global coupling factor (**Equation 1**). Therefore, strongly connected SCs require lower couplings than weak connected ones. We examined whether a similar relation exists between optimal conduction speed and features of the SC. We checked for the relation to numerous graph theoretical measure like degree, characteristic path length or average clustering of SC (weights and tract lengths) and FC, but found no significant correlation.

We were interested in the variability of our findings across the connectome. To this end, we analysed bimodality and the frequency of the neural signal of each region individually. Results are visualized in **Fig 3**, with data averaged across subjects.

Fig 3. Regional behaviour of neural signal for delta and alpha set simulations. 1st and 3rd row depicts the effect of global coupling on regional bimodality and frequency. Bimodality and fast oscillations only occur at a critical range of global coupling.(The peak in bimodality occurs at coupling values slightly higher than for the maximum frequency. 2nd and 4th row depicts the effect of conduction speed on regional bimodality and frequency. The oscillations get faster with higher speed, but bimodality is observed only for speed greater than 20 [mm/ms].

Similarly, to what we found for the global signal, regional signals at critical values of conduction speed and global coupling also shaped oscillations and bimodality. Optimal values of conduction speed occurring at the higher end of the range. Note that the averaging across the subjects and global coupling dimensions when generating **Fig 3** renders the p-values of the Hartigan's dip test of bimodality non-significant, therefore we show the percentage of subjects with bimodality (i.e. $p > 0.05$) on the colorbar. The trend of more subjects with bimodality around $G = 0.14$ (0.0295) and at conduction speeds of 60-100 mm/ms (> 20 mm/ms) in the delta (alpha) set, is indicative of the optimal parameter space that shows significant bimodality within individual subjects. At the same positions in oscillations in the respective frequency band were generated.

Within the delta set we found an interesting distribution of features across regions, with only some showing bimodal power distribution and faster oscillations. In order to understand the basis of these inter-regional differences, we

examined the relationship between degree and bimodality: We took the regional Hartigan's Dip Test p-value at optimal parameter points and plotted against the mean degree of each region. We showed that regions that have a bimodal power distribution were also strongly connected within the network, **Fig. 4 C.** Regional bimodality in anatomical space was shown in **Fig. 4 B**. Here, the nodes connected by the thickest edges (i.e. high degree) were coloured blue (i.e. bimodality). Bimodality was observed primarily along the parietal and temporal cortex ($p < 0.05$ for most of these regions). However, not all subjects at their optimal parameter combinations showed bimodality within these regions (these are the outliers in the **Fig 4 A**). At their optimal parameter point, 80% (92%) of subjects in the delta (alpha) set showed bimodal power distribution for their mean neural signal.

Fig 4. Anatomical distribution of bimodality in the delta set. A: At the optimal parameter point of each subject we assessed bimodality for all regions on the left (lh_...) and right (rh_...) hemisphere. Distribution of Hartigan's Dip Test p-values per region are shown in a boxplot. Regions are sorted from top to bottom by decreasing degree. B: 3D graph of our brain network model. To display edges, we used the mean SC across subjects, thresholded to a sparsity of 17% (i.e. showing only 17% strongest connections). Edge thickness represents the connection weight. Node colors represent the mean p-value at optimal parameter points, with blue colors indicating bimodality. C: 2D histogram showing relation between regional bimodality and mean degree. At the optimal parameter combination we assessed bimodality in each region. All graphs indicate how strongly connected brain regions observe bimodality at the optimal parameter point.

For the alpha set the regional analysis did not reveal as much of the inter-regional variation. At the optimal parameter point, nearly all regions demonstrated bimodal power distribution. Regions with number 4 and 38 are the entorhinal cortices of both hemispheres showing no bimodality. With a degree of 7.5 and 6.4 for left and right hemisphere respectively, they share the lowest degree of the whole connectome. Their activity seems to be mostly uncoupled from the rest of the system.

Mechanisms underlying alpha bimodality

Bimodality can be described as the switching of the neural signal between two modes:

One mode with high and another with low amplitude to no oscillation. Bimodality was observed in both simulation sets. The high amplitude signal oscillated with 10-14 Hz and 2-4 Hz in the alpha and delta set respectively. The low amplitude mode showed no neural oscillations. We were interested in understanding the mechanisms underlying bimodality. To this aim, we conducted further simulations where we decreased global couplings gradually in five steps to 0 (**Fig 5 and S1 Video**). At G = 0, there are no influences between nodes in the network, as we set the inter-regional

connections to 0 (the local activity at the nodes was multiplied by 0). Thus, the mean field potential was the time series generated solely by the local SJHMR3D model, without the influences of the network within which the node resides.

Fig 5. Bimodal behaviour of neural dynamics in the brain network model. Time series represent simulated neural activity in the left inferior temporal cortex of an exemplary subject. Local parameters were chosen as in the alpha set with conduction speed set to 100. Plots from top to bottom with increasing global coupling 0, 0.01, 0.025, 0.032 and 0.04. Blue time series depict the mean field potential (i.e. neural signal). Green is the global input to the inferior parietal cortex from all other nodes, scaled by connectivity weights and global coupling. On the right, the excitatory phase space is depicted with excitatory state variables x, y and z. For G = 0 it shows the switching between a limit cycle and a fixed point, creating a burst like behaviour. With increasing G the system gets more and more shifted towards the fixed point. It reaches oscillation death at G = 0.04. For G = 0.032 we have can observe a bimodal state between oscillation death (i.e. residing in the fixed point) and oscillations (i.e. limit cycling).

With the present local parameters (**Table 2**) and no global coupling, we observed a bursting behaviour in the neural signal that has been documented by the authors of the model. The burst is sometimes called square wave bursting, due to the burst shape. A fold/homoclinic bifurcation is characteristic for this type of burst, where the trajectory follows a limit cycle in the 3D phase space and generates spikes. Meanwhile the slow variable (z) increases and moves an unstable fixed point towards the limit cycle, generating a saddle homoclinic bifurcation, i.e. the unstable fixed point touches the cycle and breaks it up. The trajectory then switches towards a stable fixed point, which corresponds to the resting period. During "rest", the slow variable decreases and moves the unstable system back towards the stable fixed point creating a fold bifurcation - a transition from rest back to spiking. This bifurcation type has been described for the single Hindmarsh-Rose neuron(71), which is the foundation of the SJHMR3D.

As we increased global coupling (to G = 0.01), we began to see the impact of other regions on the local model. At a global coupling of 0.01, regions were unsynchronized, and the global input consisted of noisy fluctuations. Note that the global input range was negative (y-axis of **Fig 5**). This is because the SJHMR3D model's excitatory state variable x has a negative baseline (and positive values during spikes). When state variable x -reflecting the membrane potential of the excitatory population- was coupled with a linear scaling function to other regions of the network, it results in an inhibiting effect during baseline activity (when its values were negative) and an excitatory effect during spikes (when its values were positive). In other words, in SJHMR3d it can happen that an excitatory population *decreases or increases* the membrane potential of another neural population, depending of the current membrane potential (i.e. whether it is negative or positive).

For even higher couplings (G = 0.025), we observed a synchronization of local dynamics with global input. The regional neural signal displayed single spikes or bursts with few spikes rather than the bursting behaviour we had observed at G = 0. In the phase space there were only a few turns on the limit cycle before the homoclinic bifurcation occurs. The global input became even more negative (ie -4) than at G = 0.01. We show that the spiking in the regional neural signal actually coincided with the times at which the global input reached 0. This can be interpreted as a temporary reduction in global inhibition that leads to spikes in the local model.

For very high global coupling (G = 0.04), oscillation death occurred. The spikes and bursts were no longer present and very slow noisy fluctuations in the neural signal were observed. The neural signal and the global input had negative amplitudes and fluctuated very little. The trajectory remained at a stable fixed point.

The state of bimodality occurred in between the synchronized and the oscillation death state (G = 0.032). Namely, we observed a switching between oscillation death and spikes that occur in synchrony with a reduction in global inhibition. We show this behaviour in **S1 Video.**

Note, that the observation we made in the delta set – that there were regional differences in bimodality due to variations of regional degree, was not found in the alpha set. This may be due to differences in local parameters such as K11, K12 or σ between the two sets. It can be shown that only by changing K12, global dynamics change between unsynchronized and total synchronization, and regional differences in frequency arise (**Fig S7**).

Subject specificity

We were interested in the subject specificity of a subject's simulations, and the degree to which parameters are driven by empirical SC and FC. To determine the subject specificity of simulations, we first assessed how a subject's set of simulated FCs fits to empirical FC of other subjects (Methods). If simulations are subject specific, we would expect simulated FC to fit best to a subject's own empirical FC than to that of others. We therefore correlated the set of 105 (1510) simulated FCs in the delta (alpha) set of each subject to all subject's 50 acquired empirical FCs. This procedure yields one highest possible correlation for each pair of: subject's set of simulations, and empirical FCs. Generating a 2D matrix of size 50×50 with dimensions: being empirical FC x a subject's set of simulated FCs. The diagonal of that matrix represents the individual subject comparison, (a subject's simulated FC compared to their own empirical FC). If simulations were subject specific, we would see the highest correlation values on this diagonal.

Note that the simulated FC that fits best to the same subject's empirical FC may not necessarily be the same simulated FC that fits best to other subjects, (i.e. optimal parameter points may vary if we compare a set of simulations of one subject to empirical FCs of other subjects). We therefore extracted 50 optimal parameter points for each subject and visualized these (**Fig 6 and 7**).

Fig. 6. Cross subject comparison of simulations results. A (B): Delta set (alpha set): Left: We correlate all 105 (1510) simulations of one subject to all 50 empirical FC's. For each empirical FC we correlate to, there will be one best (i.e. highest) correlation. In other words comparing all simulations from one subject to all FC's, generates 50 highest possible correlations. Resulting in a 50*50 matrix when comparing for all 50 subjects. Along the diagonal of the matrix we find the highest possible correlation for the individual subject prediction. (i.e. predicting a subject's empirical FC by using the same subject's SC for simulation). Horizontal red and blue stripes already indicate that some empirical FC's can be predicted better than others, regardless of the SC used for the simulation. Middle: The same as the left matrix but now comparing simulations to SC, instead of empirical FC's. We test the possible prediction SC's from the simulation. A vague red diagonal indicates a best individual fit. Pointing to the fact that the simulated FC contains typical features of the used SC. Right: To test for subject specificity we now take the diagonal values (i.e. subject's individual prediction) and test their distribution against the values above and below the diagonal (i.e. all-to-all prediction). Comparing simulations to empirical FC shows no significant better individual prediction. Individual SC's can be predicted significantly better than all-to-all (two-sample Kolmogorov-Smirnoff test d = 0.4963 (d = 0.5492) and p < 0.1*10-9 (p < 0.1*10-12) for delta (alpha)). This indicates how strong the SC shapes the simulated FC. C: Left matrix shows correlation between all 50 empirical FCs. There e.g. the FC of subject #27 is very different to the rest FC, see the blue horizontal and vertical line. Right matrix is the same for SCs. The SC's seem to be much more homogeneous. Compare the high correlation coefficients on the colorbar. Middle matrix shows how similar FCs are to SC's Already without simulation some FC's can be predicted better by many SC's. E.g. see the red horizontal line for subject #29 and #35 D: Left: Scatterplot from comparison of the SC to empirical FC and empirical FC to set of simulated FCs. The better an empirical FC correlates to any given SC, the better we can predict it by simulating on that SC. Correlation r = 0.73 (r = 0.8) with p = 0 (p = 0) for delta (alpha) set. Right: Best possible individual prediction of empirical FC by SC and simulated FC, as well as SC by simulated FC. (top delta set, bottom alpha set). Simulations correlate higher to empirical FC (red) than to SC (blue). Also the prediction of the empirical FC is better with simulation rather than using the SC alone (red > green). Though we are not able to reproduce subject specific FC features, our simulations in general still compare better to functional rather than structural data.

There was no individual subject fit of simulated to empirical FCs. Individual fits (where simulated FC and empirical FC are from the same subject) are no higher than all-to-all fits (where simulated FC and empirical FC come from different subjects). Some empirical FCs correlate highly with all simulated FCs, as can be observed by the horizontal striping in the empirical FC-simulated FC plot (**Fig 6A and B left side**). That is, the goodness-of-fit is more determined by

variations in the empirical FC connectome than the simulated FC (and the underlying SC).

However, there was an individual subject fit of the SC to the simulated FC (see the stronger correlations on the diagonal o f **Fig 6 A and B middle**). This is shown also on the density distributions where individual fits (where SC and simulated FC come from the same subjects) outweigh all-to-all fits (where SC and simulated FC come from different subjects).

In order to understand the lack of subject specificity in the empirical-simulated FC fit, we examined variations between subjects' empirical FCs and also the variations between subjects' SCs (as SCs are the input to our simulations). In our SC-SC correlation and empirical FC-empirical FC correlation plots (See Fig 8C right and left), we show that empirical FCs are less homogeneous than the SCs. Thus, when we then look at the fit between individual SC and empirical FC, there was no subject-specific fit, as the fits were driven by the comparatively large variability in the empirical FC, such that there were particular empirical FCs that fit best to all SCs. Whether this is due to lower sensitivity of diffusion techniques to individual differences, or to a real lack of individual differences in SC remains to be investigated. On the other hand different success in fMRI artefact removal and processing steps could be the reason for different FC quality.

There is a linear relation between the fit of empirical FC to SC and the fit of simulated to empirical FC (**Fig 6D left**). Correlations between empirical SC and FC, empirical SC with simulated FC and simulated and empirical FC are shown in **Fig 6D right**. For both sets, we see the correlation between individual SC and empirical FC (green) is lower than that of simulated to empirical FCs (red). In other words, by using the SC only we cannot predict the empirical FC as good as by using the SC in a simulation. That is the value added by TVB. Although simulated FC fit specific to their underlying SC they still fit better to their empirical counterpart (blue < red). Meaning the combination of SC and our model is more like a FC than an SC.

Another interesting aspect of this inter subject comparison is the variance of the optimal parameters (**Fig 7**). Here we ask the question, what are the optimal parameters for a set of simulations (i.e. the underlying SC). Does the optimal point change when correlating to different empirical FCs? Are optimal parameters determined by the underlying SC or the empirical FC we compare to? The variation of optimal global coupling within a set of simulation is small compared to the variation between sets (**Fig 7A**). As we've shown earlier the global coupling relies on the weights supplied by the SC. In combination with the mechanism of bimodality it makes sense that regardless of the FC we compare to, the optimal global coupling has to stay in a close range because otherwise the local dynamics will generate unphysiological/ a non-meaningful signal. In other words, the explained variation of global coupling by the underlying SC is great. Whereas for conduction speed the inter and intra subject variation is high.

Fig 7. Optimal parameter combinations of cross subject comparison. A. Comparing all simulations of one subject to its own empirical FC yields one optimal parameter combination. However, this parameter combination doesn't have to be optimal in terms of goodness of fit if we compare the same set of simulations to the empirical FC of other subjects. In other words when we correlate the simulations of one subject to all 50 empirical FC's we will get 50 optimal parameter combinations – one for each subject's empirical reference FC. Doing this for all 50 subjects yields 50×50 optimal parameter combinations and highest correlations. The matrices of correlation are displayed in Fig 8. B. Next, we analyse how these optimal parameter distributions change in-between subjects. The parameters are influenced by the set of simulations (i.e. underlying SC) if the distribution means vary strongly in-between them. This can be seen for optimal global coupling in the upper boxplot. The variance within one set of simulation is small compared to the variance between them. If we transpose the 50×50 optimal parameter matrix we can analyse the influence of the empirical FC on the distributions. Empirical FC doesn't influence the parameter distribution strongly. This Fig indicates the high importance of the SC on optimal coupling determination regardless of the empirical FC we are trying to fit. Optimal conduction speed (not shown here) however doesn't seem to be determined by SC or FC, as the variance between subjects in A and B is small.

To assess if optimal parameters are more determined by the set of simulations (in other words underlying SC) or by the empirical FC we have to ask the reverse questions: How do optimal parameters vary across empirical FCs and is this variation greater or smaller than the one before. To do that, we transpose the boxplot with the x-axis now being empirical FCs. We see the within one empirical FC variation of coupling and speed is large and the between variation small. In other words, the explained variation of parameters by empirical FC is small. The plots in **Fig 7** can be shown for the delta set too, with similar but smaller trends.

Now we want to quantify if the underlying SC or the empirical FC determines optimal parameters. Therefore, we use the eta squared effect size which is computed as the ratio of sum of squares between groups and sum of squares total using the boxplot in **Fig 7**. This metric will have values between 0 (no variance explained by the variable) and 1 (variance completely explained) (**Table 4)**.

Table 4: Eta squared. Explained variance of optimal parameters by empirical FC and the simulations underlying SC for both set.

	Delta set		**Alpha set**	
Explained variance	by underlying SC	by empirical FC	by underlying SC	by empirical FC
for global coupling	0.4629	0.2826	0.7968	0.0175
for conduction speed	0.0735	0.0913	0.0989	0.0809

Optimal coupling is mostly determined by the underlying SC. The effect is more visible in the alpha set with an eta

squared of 0.7968 for coupling explained by SC compared to 0.0175 by empirical FC. Also, delta set shows same characteristics with small differences in effect sizes.

Our question could be asked in a different way: Are there specific features in an empirical FC that can only be reproduced by a certain set of parameter combinations? The answer would be no for global coupling. The parameter is more or less bound to the underlying SC to generate meaningful simulations. However, conduction speed is neither determined by the SC nor by empirical FC. At this point we cannot give an explanation why optimal conduction speed differs between subjects. However the change in simulation result is very small for different conduction speed. So that a variety of transmission speeds can be seen as optimal.

FCD

In order to investigate FCDs in our model we conducted simulations of 22 min lengths. Due to long computation times we limited the exploration to four exemplary subjects (gender/age: f/30, f/47, m/20, m/73). Parameters where chosen from the alpha set with conduction speed set to the individual optimal value (derived from analysis in alpha set section).

In **Fig 8** an empirical and a simulated FCD are shown. It is visible that there are recurrent patterns in the recorded BOLD signal creating time shifted but highly correlated FCs. The same can be observed in our simulation. Though highest correlations are lower than in the empirical data. Interestingly FCD fit, bimodality and static FC fit are highly correlated. They all show their optimum in the same range of global coupling. Meaning that only when our local model is in a bistable situation we are able to generate switching of modes in our global network. In our supplementary material **S2 Video** we show simulated and empirical FCDs and FCs for subject #2 while sliding across the range of global coupling values.

Fig. 8. Functional connectivity dynamics aligns with bimodal behaviour of neural dynamics A: Shows example empirical and simulated FCD of Subject #2. B: Metrics of 22 minutes simulations for four sample subjects. In blue the Kolmogorov-Smirnoff distance between the simulated and empirical FCD. Best FCD fit occurs at the same range of global coupling as bimodality of the global signal (green) and best fit between FC's (red).

Discussion

In the current study, we conducted a large parameter space exploration with TVB, simulating BOLD fMRI and electrophysiological neural signals for 50 individual human brains. TVB has previously been used to study how neural networks behave in healthy and diseased states (8,10,13,18,21,26). Here, we assert that goodness-of-fit of simulated to empirical data converge at a particular parameter set across multiple tenets of the EEG and fMRI signal, and that there are reliable inter-individual differences in biophysical parameters that lead to optimal functioning. In order to understand the behaviour of the system at multiple time scales, we conducted two sets of simulations, one that shows neural behaviour in the delta frequency range, and a second that shows alpha oscillations.

It has been shown that the space-time formation of the dynamic repertoire of the neural system arises from a combination of the structural connectome, and the time delays determined by conduction speed with which the signal propagates across the anatomical skeleton(26,72–75). The global coupling and the conduction speed capture the influence of the structural backbone and the time delays, respectively, and were the two free parameters of interest in the current study.

The global coupling is responsible for the balance between local (nodal behaviour described by the SJHMR3D model) and global (network-level) dynamics of the system, by scaling the SC connection weights. The conduction speed defines the speed of signal propagation across the structural connectome.

Importantly, minute variations in these parameters were shown to give rise to fluctuations in 1) the correlation between empirical and simulated BOLD FC, 2) frequency of the mean neural signal, as well as 3) bimodality in the frequency power in the alpha band, a feature that has been observed in empirical (37,38), and model (42) EEG data. 4) fit of FCD (characterized as KS distance between simulated and empirical FCD). These features converge at a particular parameter point unique to each subject. Typically, a single metric (typically a correlation between empirical and simulated FC) is used to assess model fit. Yet, it is important to validate that optimal models converge across multiple metrics and modalities.

Biological interpretation of SJHM3D based BNMs

SJHMR3d primarily aims to describe the average membrane potential of a population of neurons that are electrically coupled via gap junction (19). On a local scale, this is achieved via difference coupling: the input that an excitatory (respectively inhibitory) neuron receives is the difference between the neuron's membrane potential and the mean field of the excitatory (respectively inhibitory) subpopulation. That is, inputs are based on the difference between a neuron's state and the average state of all presynaptic neurons, instead of being based on the sum of presynaptic neurons' states.

This leads to a situation where an excitatory population can decrease the membrane potential of a postsynaptic neuron and an inhibitory neuron can increase the membrane potential of a postsynaptic neuron, which simulates the behaviour of electrical coupling via gap junctions, but not coupling via chemical synapses with neurotransmitters like NMDA, AMPA and GABA, which are either only excitatory or only inhibitory. For a demonstration see our **S1 Video**, where excitatory large-scale coupling leads to inhibitory inputs to individual brain regions over the majority of time in all simulations. In (76) an example is shown of how chemical synapses can be implemented in a Hindmarsh-Rose neuron in a way that biological plausibility is maintained. There, in Equation 14 a sigmoidal function is used for chemical coupling, which is set up, such that coupled values are always positive. This ensures that excitatory neurons always excite and inhibitory neurons always inhibit. In the present study, the SJHMR3D model was used on the local scale, and regions were coupled using a linear scaling function on the global scale. For such a scenario, due to the reasons discussed above, claims made about the SJHMR3D regarding GABAergic or NMDAergic neurotransmission are not justified. Conclusions about NMDA and GABA neurotransmission and about local disinhibition etc. cannot be drawn from a model like SJHMR3d that represents electrical coupling between neurons. This needs to be kept in mind when running TVB simulations with SJHMR3d.

Biological meaning of biophysical model parameters

Conduction speed: Our range of conduction velocities (10-100m/s) was comparable to that found in the adult primate brain (5-94m/s), where neural axons were heavily biased towards those with large diameters and high conduction speeds(77). Similarly, we found that features of our empirical signal were best reproduced at conduction velocities higher than 20 mm/ms. ***Global coupling:*** Optimal global coupling is largely dependent on the underlying SC (78), which varies across studies that have used this connectivity scaling factor(22,25,73,74,79). For instance, our global coupling factor was quite low, and comparable to studies with dense SCs due to coarse parcellation schemes (Results: delta set ~0.13, alpha set ~ 0.03). Previous results for global coupling ~0.007 (22), ~0.016 (73), ~0.3-0.9(69).

Role of biophysical parameters for model fit

We found that the ability of the model to approximate the empirical neural signal (in correlation, mean frequency, and bimodality of the frequency power spectrum at the alpha band) was determined predominantly by the global coupling, and less by the conduction velocity; such that, for example, the highest correlation between the FCs occurred at a small range of couplings, but across a wide range of conduction speeds. Previous resting-state models have all emphasized the critical role of the inter-nodal coupling in determining spatial structure(22,72–74,79,80); whereby the effects of delays are determined by local dynamics. Spiking models (30) such as the Deco Wong Wang, in contrast with simple oscillators (22,74,80), may not necessitate time delays, as synchronization is decreased through system heterogeneity,

noise, and greater time between individual spikes(30). Oscillatory dynamics (75), but not slow asynchronous dynamics (81) are influenced by time delays. Moreover, delays have a greater influence on dynamics in directed (asymmetric) graphs, than undirected symmetric networks (78) such as our diffusion SCs. This is because real symmetric matrices will have real eigenvalues, thus the connectivity will affect the system's equilibrium, however not its dynamic oscillatory behaviour (78). The Hindmarsh-Rose local neural model is similar to the FitzHugh-Nagumo, where time delays were not critical in shaping network dynamics. Critical behaviours are independent of very high conduction velocities that correspond to time delays approaching zero, which is the case in the present study.

Coupling, on the other hand, is important in determining the coordinated behaviour of the system. With low coupling values, nodal models are largely disconnected, their behaviour independent of one another, resulting in low signal correlations and little synchronization throughout the system. As coupling increases, inter-regional influences are taken into account in the network dynamics. Increasing the coupling beyond a certain critical threshold point was found to drastically change the system behaviour, where too much synchrony results in waning bimodality, for example. Thus, an intermediate coupling may best represent the realistic influence of inter-nodal inputs.

Importantly, we found that optimal coupling decreased with increasing average SC weights. We explain these results as follows: In order to realistically model local dynamics within one node, a certain amount of input from other nodes is needed. Therefore, if the SC weights are low, a sufficient high global coupling value is necessary to scale up the input from other nodes. A link between coupling and global efficiency in the SC has previously been reported (8), yet the association to mean SC has not yet been clearly emphasized. This is important, as using SJHMR3D and similar models to make interpretations about clinical populations rest on the comparison of SCs that vary greatly across individuals.

The realistic properties of the simulated neural signal that we found, do not arise linearly with global coupling, but rather slowly emerge or strengthen, sharply peak, and drop off afterwards. Interestingly, a number of other resting-state neural network properties, such as system multistability (25), changes in the attractor landscape (the entropy and number of attractors)(32,81), cluster synchronization(22,74), emergence of resting state networks (72,74), instability of the equilibrium state(73,78), system efficiency(8), or network entropy (82), have similarly been shown to develop and transition as a function of this inter-regional coupling, conduction velocity, or a combination of the two (22,73,74,78). Similarly to what we noticed in our study, these behaviours actually emerge at the point where global coupling produces the highest correlation between empirical and simulated FC. Taken together, these findings point to the significance of a critical point at which the system performs/operates/functions optimally. Note that noise, among other parameters, may

additionally influence the emergence of these features (22), however, may not be necessary for resting-state fluctuations(74).

Role of biophysical parameters for functional connectivity dynamics

Recently, it has been shown that functional connectivity fluctuates across time, and that functional connectivity dynamics emphasize important features of the signal that cannot be captured by the static FC(66,83). Static FC is the FC from a single time series, while dynamic FC is characterized as changing patterns in the FC captured by correlating numerous FCs from sub-windows of the time series. We verified that non-static FCD is observed at the bimodal state. In particular, we showed that the region of parameter space that gives rises to the best fit between simulated and empirical static FC, and bimodality, also gives rise to the best model of FCD. This is important, as we are able to show that our simulations can reproduce time-varying features of the signal which are relevant to capturing individual differences (63), and other resting-state phenomena(34). Our findings are in line with previous findings showing the meta-stable state as a function of a bifurcation parameter called "a" along with global coupling, and importantly, that best FCD fit is achieved at this meta-stable state(34).

Role of biophysical parameters for frequency and alpha bimodality

In a second set of simulations, we explored a narrower range of global coupling and reproduced alpha frequency (8-15 Hz) oscillations in the neural signal, a characteristic feature of human empirical EEG (37,38), which has previously been modelled as a function of global coupling in MEG (30). Here, it was shown that transmission delays and global cortical coupling affect the mean power in an MEG model, and the best model fit was found in the alpha band power. However, this work is limited to the traditional mean power metric, without taking into account the bistable switching between two distinct alpha modes that occurs in empirical neural signal. We found that global coupling that exceeded a certain threshold led to a sharp reduction in oscillation frequency to a predominantly delta frequency range with low amplitude.

Because the mean power metric that is commonly reported in frequency analyses lacks information about fluctuations around the mean, we also examined the distribution of the frequency power. We were able to reproduce bistable switching between two distinct alpha modes, a feature of empirical EEG (37,38). The two modes (a low power mode and a high-power mode) represent the switching, or bursting, between two distinct dynamic behaviours within a cortical region. The non-Gaussian, multistable nature of these neural processes should be taken into account in any realistic neural model, however, has largely been overlooked. We show that this bimodality, which has previously been modelled

as a function of noise (42), arises also as a function of optimal global coupling. It is reasonable that the long-range inter-nodal global connections shape the bimodality particularly of the mean global neural signal. This can be contrasted with previous studies (42), where bimodality was modelled on the neural signal of a single node, thus global parameters would likely not play a large role in determining the behaviour. Further, note that the optimal working point where bimodality emerges is the same one that gives rise to high correlations between simulated and empirical FC, as well as FCD, suggesting that realistic modelling of empirical data can be attained in a particular parameter space.

Mechanisms underlying alpha bimodality

We sought to elucidate the mechanisms behind the emergence of bimodality in our model. Bimodality was shown as a function of the global coupling parameter. For low values of global coupling, (i.e. G = 0), we observed bursting behavior at the local model (local dynamics dominate, as the coupling from other regions is 0). Such square-wave bursting behavior, as well as single spikes and chaotic behaviour, have been observed in the SJHMR3D and the single Hindmarsh-Rose model (19,71). As we then increase global coupling, a synchronized state is achieved, such that many regions show synchronized spiking behavior. Increasing global coupling yet further results in the bimodality we observe, and finally, oscillation death.

These changes can be understood by looking at our global coupling function. The current SJHMR3D model uses the linear coupling function of the form: "$x_i = a * x_j + b$", where "x_i" is the value that gets integrated in the local model and "x_j" is the activity at other regions with some time delay. "a" is the global coupling factor that scales the activity of the other regions and "b" = 0 in our case. In our SJHMR3D model, the state variable "x" (activity of excitatory neurons) gets transmitted in the global network. This corresponds to a biological global excitatory coupling in the brain.

The baseline of this variable is around -2 [a.u.] corresponding to a neuron at rest, while spikes peak at +2 [a.u.]. At rest, this negative value is the "x_j" of a region that gets transmitted throughout our network. Thereby we create global inhibition. Thus, at low values of global coupling, bursts/spikes still occur at a node as global inhibition is not strong enough to suppress this activity. However, as we increase global coupling, we increase global inhibition up to a point where inhibition is strong enough to cancel out all activity. In between, there is a narrow range of coupling values where a switching between periods of spiking behaviour and periods of oscillation death can be observed, giving rise to a bimodal power distribution. Taking into account that different nodes have different degrees, we can explain that some nodes reach bimodality and oscillation death earlier than others. Thus, inter-regional input plays an important role in

driving oscillatory activity, as seen previously in the alpha band (30).

In follow-up studies, we will seek to understand the impact of a different global coupling function, a sigmoidal/hyperbolic tangent function, to avoid global inhibition and oscillation death.

Inter-individual differences.

We show that there are inter-individual differences in the optimal long-range global coupling that result in the best fit between the empirical and simulated functional connectome, in predominating alpha frequencies of the neural signal, and bimodality in the frequency power spectrum at the alpha range. The critical value at which these behaviours emerge and the simulated-empirical FC correlation is the highest is consistent across behaviours, and varies reliably across subjects. This suggests that the optimal point of functioning is highly dependent on the individual's anatomical architecture in combination with the spatio-temporal dynamics from the model. Our findings indicate the importance of conducting parameter space explorations at the individual level, as more standard group-level analyses (32,74) may obscure important and reliable variability. Moreover, we show that individual variability in the connectomes was driven primarily by the simulated FC, and the underlying SC, and to a lesser extent by the empirical FC. This is important if one starts to simulate or explore parameters for a subject. Typically, we have empirical data such as fMRI FC and DTI derived SC but we do not know what parameter values to choose. The best orientation for optimal global coupling can be drawn from the SC rather than the empirical FC. The same cannot be said for conduction velocity. There may be other parameters we didn't explore which may be determined more by the empirical FC rather than the SC.

The simulated-empirical FC correlations (*delta set*: mean r = 0.45; max r = 0.66; *alpha set*: mean r = 0.51, max r = 0.68) that we achieve are in the range of those obtained in parameter explorations with similar models (74,82) (r = 0.427); (32)(r = 0.42); (25)(r = ~0.4). It is important to note that the ability of our model to reproduce the empirical data is limited by the quality of current diffusion techniques. Existing links that are not captured by the SC may conceal how real structural connections influence FC. However, in light of these inherent limitations, our model has captured a number of important properties of the neural and BOLD signal.

In sum, we have demonstrated that as global coupling and conduction speed approach an optimal working point, the behaviour of the neural system maximally reproduces the resting-state BOLD static and dynamic FC, as well as the neural signal.

Taken together, The Virtual Brain is a neuroinformatics platform that allows reproducible computational brain modelling. With the present work, we aim to provide guidance for personalized brain network modelling using SJHMR3D nodes. Example data sets, code and didactic video tutorials for published TVB studies are being made available as didactic use cases (84). A systematic exploration of other population models and comparisons of their respective parameter landscapes will help to further put to test and to validate the biological interpretability of parameters and variables of those models (85).

Acknowledgements

We gratefully acknowledge the Gauss Centre for Supercomputing e.V. (www.gauss-centre.eu) for funding this project by providing computing time through the John von Neumann Institute for Computing (NIC) on the GCS Supercomputer JUWELS at Jülich Supercomputing Centre (JSC). Additionally, computation has also been performed on the HPC for Research cluster of the Berlin Institute of Health. We thank Michael Schirner for insightful discussions.

P.R. acknowledges the following funding sources: James S. McDonnell Foundation, H2020 Research and Innovation Action grants VirtualBrainCloud 826421, Human Brain Project 785907 and ERC 683049; German Research Foundation CRC 1315, CRC 936 and RI 2073/6-1; Berlin Institute of Health & Foundation Charité, Johanna Quandt Excellence Initiative.

References

1. Breakspear M. Dynamic models of large-scale brain activity. Nat Neurosci. 2017;20(3):340–52.
2. Woodman MM, Pezard L, Domide L, Knock SA, Sanz-Leon P, Mersmann J, et al. Integrating neuroinformatics tools in TheVirtualBrain. Front Neuroinform. 2014;8:36.
3. Sanz Leon P, Knock SA, Woodman MM, Domide L, Mersmann J, McIntosh AR, et al. The Virtual Brain: a simulator of primate brain network dynamics. Front Neuroinform. 2013;7:10.
4. Stefanovski L, Ghani A, McIntosh AR, Ritter P. Linking connectomics and dynamics in the human brain. e-Neuroforum. 2016;7(3):64–70.
5. Deco G, Kringelbach ML, Jirsa VK, Ritter P. The dynamics of resting fluctuations in the brain: Metastability and its dynamical cortical core. Sci Rep. 2017;7(1):1–14.
6. Schirner M, McIntosh AR, Jirsa V, Deco G, Ritter P. Inferring multi-scale neural mechanisms with brain network modelling. Elife. 2018;7:1–30.
7. Ritter P, Schirner M, McIntosh AR, Jirsa VK. The virtual brain integrates computational modeling and multimodal neuroimaging. Brain Connect [Internet]. 2013;3(2):121–45. Available from: http://www.pubmedcentral.nih.gov/articlerender.fcgi?artid=3696923&tool=pmcentrez&rendertype=abstract
8. Falcon MI, Riley JD, Jirsa V, McIntosh AR, Shereen AD, Chen EE, et al. The Virtual Brain: Modeling Biological Correlates of Recovery after Chronic Stroke. Front Neurol. 2015;6:228.
9. Falcon MI, Riley JD, Jirsa V, McIntosh AR, Chen EE, Solodkin A. Functional Mechanisms of Recovery after Chronic Stroke: Modeling with the Virtual Brain. eNeuro. 2016;3(2).
10. Adhikari MH, Raja Beharelle A, Griffa A, Hagmann P, Solodkin A, McIntosh AR, et al. Computational modeling of resting-state activity demonstrates markers of normalcy in children with prenatal or perinatal stroke. J Neurosci. 2015;35(23):8914–24.
11. Aerts H, Schirner M, Jeurissen B, Van Roost D, Achten E, Ritter P, et al. Modeling Brain Dynamics in Brain Tumor Patients Using the Virtual Brain. Eneuro. 2018;5(3):ENEURO.0083-18.2018.
12. Aerts H, Dhollander T, Achten E, Marinazzo D. Modeling brain dynamics after tumor resection using The Virtual Brain. Front Neurosci [Internet]. 2019;13(February):116738. Available from: https://doi.org/10.1016/j.neuroimage.2020.116738
13. Falcon MI, Jirsa V, Solodkin A. A new neuroinformatics approach to personalized medicine in neurology: The Virtual Brain. Curr Opin Neurol. 2016;29(4):429–36.
14. Proix T, Jirsa VK. Using the connectome to predict epileptic seizure propagation in the human brain. BMC Neurosci [Internet]. 2015;16(Suppl 1):P110. Available from: http://www.biomedcentral.com/1471-2202/16/S1/P110
15. Jirsa VK, Proix T, Perdikis D, Woodman MM, Wang H, Gonzalez-Martinez J, et al. The Virtual Epileptic Patient: Individualized whole-brain models of epilepsy spread. Neuroimage [Internet]. 2015;145:377–88. Available from: http://dx.doi.org/10.1016/j.neuroimage.2016.04.049
16. Kunze T, Hunold A, Haueisen J, Jirsa V, Spiegler A. Transcranial direct current stimulation changes resting state functional connectivity: A large-scale brain network modeling study. Neuroimage. 2016;140:174–87.
17. Roy D, Sigala R, Breakspear M, McIntosh AR, Jirsa VK, Deco G, et al. Using the virtual brain to reveal the role of oscillations and plasticity in shaping brain's dynamical landscape. Brain Connect. 2014;4(10):791–811.
18. Ritter P, Schirner M, McIntosh AR, Jirsa VK. The virtual brain integrates computational modeling and multimodal neuroimaging. Brain Connect. 2013;3(2):121–45.

19. Stefanescu R, Jirsa VK. A low dimensional description of globally coupled heterogeneous neural networks of excitatory and inhibitory neurons. PLoS Comput Biol. 2008;4(11).

20. Deco G, McIntosh AR, Shen K, Hutchison RM, Menon RS, Everling S, et al. Identification of optimal structural connectivity using functional connectivity and neural modeling. J Neurosci [Internet]. 2014;34(23):7910–6. Available from: http://www.ncbi.nlm.nih.gov/pubmed/24899713%5Cnhttp://www.jneurosci.org/content/34/23/7910.full.pdf

21. Kringelbach ML, McIntosh AR, Ritter P, Jirsa VK, Deco G. The Rediscovery of Slowness: Exploring the Timing of Cognition. Trends Cogn Sci. 2015;19(10):616–28.

22. Deco G, Jirsa V, McIntosh AR, Sporns O, Kotter R. Key role of coupling, delay, and noise in resting brain fluctuations. Proc Natl Acad Sci U S A. 2009/06/06. 2009;106(25):10302–7.

23. Deco G, Ponce-Alvarez A, Hagmann P, Romani G., Mantini D, Corbetta M. How local excitation-inhibition ratio impacts the whole brain dynamics. J Neurosci [Internet]. 2014;34(23):7886–98. Available from: http://www.pubmedcentral.nih.gov/articlerender.fcgi?artid=4044249&tool=pmcentrez&rendertype=abstract

24. Waxman SG. Determinants of conduction velocity in myelinated nerve fibers. Muscle Nerve. 1980;3(2):141–50.

25. Deco G, Jirsa VK, McIntosh AR. Resting brains never rest: Computational insights into potential cognitive architectures. Trends Neurosci. 2013;36(5):268–74.

26. Jirsa VK, Stacey WC, Quilichini PP, Ivanov AI, Bernard C. On the nature of seizure dynamics. Brain. 2014;137(Pt 8):2210–30.

27. Zimmermann J, Perry A, Breakspear M, Schirner M, Sachdev P, Wen W, et al. Differentiation of Alzheimer's disease based on local and global parameters in personalized Virtual Brain models. NeuroImage Clin [Internet]. 2018;19(April):240–51. Available from: https://doi.org/10.1016/j.nicl.2018.04.017

28. Stefanovski L, Triebkorn P, Spiegler A, Arimatea M-. Linking molecular pathways and large- – scale computational modeling to assess candidate disease mechanisms and pharmacodynamics in Alzheimer ' s disease. 2019;1–46.

29. Solodkin A, Zimmermann J, McIntosh AR, Stefanovski L, Ritter P. Neurological Biomarkers and Neuroinformatics [Internet]. Molecular-Genetic and Statistical Techniques for Behavioral and Neural Research. Elsevier Inc.; 2018. 3–30 p. Available from: http://dx.doi.org/10.1016/B978-0-12-804078-2.00001-5

30. Nakagawa TT, Woolrich M, Luckhoo H, Joensson M, Mohseni H, Kringelbach ML, et al. How delays matter in an oscillatory whole-brain spiking-neuron network model for MEG alpha-rhythms at rest. Neuroimage [Internet]. 2014;87:383–94. Available from: http://dx.doi.org/10.1016/j.neuroimage.2013.11.009

31. Deco G, Rolls ET, Romo R. Stochastic dynamics as a principle of brain function. Prog Neurobiol. 2009;88(1):1–16.

32. Deco G, Jirsa VK. Ongoing Cortical Activity at Rest: Criticality, Multistability, and Ghost Attractors. J Neurosci. 2012;32(10):3366–75.

33. Ghosh A, Rho Y, McIntosh AR, Kotter R, Jirsa VK. Noise during rest enables the exploration of the brain's dynamic repertoire. PLoS Comput Biol. 2008;4(10):e1000196.

34. Deco G, Kringelbach ML, Jirsa V, Ritter P. The dynamics of resting fluctuations in the brain: metastability and its dynamical cortical core. bioRxiv [Internet]. 2016;065284. Available from: http://biorxiv.org/lookup/doi/10.1101/065284

35. Díaz-parra A, Osborn Z, Canals S, Moratal D, Sporns O. Structural and functional, empirical and modeled connectivity in the cerebral cortex of the rat. Neuroimage [Internet]. 2017;159(July):170–84. Available from: http://dx.doi.org/10.1016/j.neuroimage.2017.07.046

36. Shen K, Bezgin G, Schirner M, Ritter P, Everling S, McIntosh AR. A macaque connectome for large-scale network simulations in TheVirtualBrain. Sci data [Internet]. 2019;6(1):123. Available from: http://dx.doi.org/10.1038/s41597-019-0129-z

37. Freyer F, Aquino K, Robinson PA, Ritter P, Breakspear M. Bistability and non-Gaussian fluctuations in spontaneous cortical activity. J Neurosci. 2009;29(26):8512–24.

38. Freyer F, Roberts JA, Becker R, Robinson PA, Ritter P, Breakspear M. Biophysical mechanisms of multistability in resting-state cortical rhythms. J Neurosci. 2011;31(17):6353–61.

39. Becker R, Ritter P, Villringer A. Influence of ongoing alpha rhythm on the visual evoked potential. Neuroimage. 2008;39(2):707–16.

40. Reinacher M, Becker R, Villringer A, Ritter P. Oscillatory brain states interact with late cognitive components of the somatosensory evoked potential. J Neurosci Methods. 2009;183(1):49–56.

41. Becker R, Reinacher M, Freyer F, Villringer A, Ritter P. How ongoing neuronal oscillations account for evoked fMRI variability. J Neurosci. 2011;31(30):11016–27.

42. Freyer F, Roberts JA, Ritter P, Breakspear M. A canonical model of multistability and scale-invariance in biological systems. PLoS Comput Biol. 2012;8(8):e1002634.

43. Becker R, Knock S, Ritter P, Jirsa V. Relating Alpha Power and Phase to Population Firing and Hemodynamic Activity Using a Thalamo-cortical Neural Mass Model. PLoS Comput Biol. 2015;11(9):1–23.

44. Sigala R, Haufe S, Roy D, Dinse HR, Ritter P. The role of alpha-rhythm states in perceptual learning: insights from experiments and computational models. Front Comput Neurosci. 2014;8:36.

45. Ritter P, Born J, Brecht M, Dinse HR, Heinemann U, Pleger B, et al. State-dependencies of learning across brain scales. Front Comput Neurosci. 2015;9(FEB):1–21.

46. Chiang AK, Rennie CJ, Robinson PA, van Albada SJ, Kerr CC. Age trends and sex differences of alpha rhythms including split alpha peaks. Clin Neurophysiol. 2011;122(8):1505–17.

47. Moosmann M, Ritter P, Krastel I, Brink A, Thees S, Blankenburg F, et al. Correlates of alpha rhythm in functional magnetic resonance imaging and near infrared spectroscopy. Neuroimage. 2003;20(1):145–58.

48. Ritter P, Moosmann M, Villringer A. Rolandic alpha and beta EEG rhythms' strengths are inversely related to fMRI-BOLD signal in primary somatosensory and motor cortex. Hum Brain Mapp. 2009;30(4):1168–87.

49. Schirner M, Rothmeier S, Jirsa VK, McIntosh AR, Ritter P. An automated pipeline for constructing personalized virtual brains from multimodal neuroimaging data. Neuroimage. 2015;117:343–57.

50. Desikan RS, Segonne F, Fischl B, Quinn BT, Dickerson BC, Blacker D, et al. An automated labeling system for subdividing the human cerebral cortex on MRI scans into gyral based regions of interest. Neuroimage. 2006;31(3):968–80.

51. Smith RE, Tournier JD, Calamante F, Connelly A. Anatomically-constrained tractography: improved diffusion MRI streamlines tractography through effective use of anatomical information. Neuroimage. 2012;62(3):1924–38.

52. Welvaert M, Rosseel Y. On the definition of signal-to-noise ratio and contrast-to-noise ratio for FMRI data. PLoS One. 2013;8(11):e77089.

53. Bezgin G, Solodkin A, Bakker R, Ritter P, McIntosh AR. Mapping complementary features of cross-species structural connectivity to construct realistic "virtual brains." Hum Brain Mapp. 2017;38(4):2080–93.

54. Friston KJ. Statistical parametric mapping: Ontology and current issues. J Cereb Blood Flow Metab. 1995;15(361–370).

55. Hindmarsh JL, Rose RM. A model of neuronal bursting using three coupled first order differential equations.

Vol. 221, Proceedings of the Royal Society of London B: Biological Sciences. 1984. p. 87–102.

56. Team RC. R: A language and environment for statistical computing. Vienna, Austria: R Foundation for Statistical Computing; 2014. 2014.

57. Jones E, Oliphant T, Peterson P. {SciPy}: open source scientific tools for {Python}. 2014;

58. Beckmann CF, DeLuca M, Devlin JT, Smith SM. Investigations into resting-state connectivity using independent component analysis. Philos Trans R Soc London B Biol Sci. 2005/08/10. 2005;360(1457):1001–13.

59. Esposito F, Bertolino A, Scarabino T, Latorre V, Blasi G, Popolizio T, et al. Independent component model of the default-mode brain function : Assessing the impact of active thinking. 2006;70:263–9.

60. Bassett DS, Wymbs NF, Porter MA, Mucha PJ, Carlson JM, Grafton ST. Dynamic reconfiguration of human brain networks during learning. Proc Natl Acad Sci . 2011 May;108(18):7641–6.

61. Horovitz SG, Fukunaga M, de Zwart JA, van Gelderen P, Fulton SC, Balkin TJ, et al. Low frequency BOLD fluctuations during resting wakefulness and light sleep: a simultaneous EEG-fMRI study. Hum Brain Mapp. 2007/06/29. 2008;29(6):671–82.

62. Boveroux Pierre MD, Vanhaudenhuyse Audrey BS, Bruno Marie-Aurélie BS, Noirhomme Ph.D. ,Quentin I, Lauwick Séverine MD, Luxen André PD, et al. Breakdown of within- and between-network Resting State Functional Magnetic Resonance Imaging Connectivity during Propofol-induced Loss of Consciousness. Anesthesiology. 2010 Nov;113(5):1038–53.

63. Battaglia D, Thomas B, Hansen ECA, Chettouf S, Daffertshofer A, McIntosh AR, et al. Functional Connectivity Dynamics of the Resting State across the Human Adult Lifespan. bioRxiv. 2017;

64. Damaraju E, Allen EA, Belger A, Ford JM, Mcewen S, Mathalon DH, et al. Clinical Dynamic functional connectivity analysis reveals transient states of dysconnectivity in schizophrenia. Neuroimage [Internet]. 2014;5(July):298–308. Available from: http://dx.doi.org/10.1016/j.nicl.2014.07.003

65. Jones DT, Vemuri P, Murphy MC, Gunter JL, Senjem ML, Machulda MM, et al. Non-Stationarity in the "Resting Brain's" Modular Architecture. He Y, editor. PLoS One. 2012 Jun;7(6):e39731.

66. Hansen EC, Battaglia D, Spiegler A, Deco G, Jirsa VK. Functional connectivity dynamics: modeling the switching behavior of the resting state. Neuroimage. 2015;105:525–35.

67. Sui J, Huster R, Yu Q, Segall JM, Calhoun VD. Function-structure associations of the brain: evidence from multimodal connectivity and covariance studies. Neuroimage. 2014;102 Pt 1:11–23.

68. Khalsa S, Mayhew SD, Chechlacz M, Bagary M, Bagshaw AP. The structural and functional connectivity of the posterior cingulate cortex: comparison between deterministic and probabilistic tractography for the investigation of structure-function relationships. Neuroimage. 2014;102 Pt 1:118–27.

69. Honey CJ, Kotter R, Breakspear M, Sporns O. Network structure of cerebral cortex shapes functional connectivity on multiple time scales. Proc Natl Acad Sci U S A. 2007;104(24):10240–5.

70. Sporns O. Structure and function of complex brain networks. Dialogues Clin Neurosci. 2013;15(3):247–62.

71. Barrio R, Mart??nez MA, Serrano S, Shilnikov A. Macro- and micro-chaotic structures in the Hindmarsh-Rose model of bursting neurons. Chaos. 2014;24(2):023128.

72. Ghosh A, Rho Y, McIntosh AR, Kötter R, Jirsa VK. Cortical network dynamics with time delays reveals functional connectivity in the resting brain. Cogn Neurodyn. 2008;2(2):115–20.

73. Ghosh A, Rho Y, McIntosh AR, Kotter R, Jirsa VK. Noise during Rest Enables the Exploration of the Brain's Dynamic Repertoire. PLoS Comput Biol. 2008;4(10):e1000196.

74. Cabral J, Hugues E, Sporns O, Deco G. Role of local network oscillations in resting-state functional

connectivity. Neuroimage. 2011;57(1):130–9.

75. Jirsa VK. Neural field dynamics with local and global connectivity and time delay. Philos Trans A Math Phys Eng Sci. 2009;367(1891):1131–43.

76. Majhi S, Bera BK, Ghosh D, Perc M. Chimera states in neuronal networks: A review. Phys Life Rev [Internet]. 2019;28:100–21. Available from: https://doi.org/10.1016/j.plrev.2018.09.003

77. Firmin L, Field P, Maier MA, Kraskov A, Kirkwood PA, Nakajima K, et al. Axon diameters and conduction velocities in the macaque pyramidal tract. J Neurophysiol. 2014;112(6):1229–40.

78. Knock SA, McIntosh AR, Sporns O, Kotter R, Hagmann P, Jirsa VK. The effects of physiologically plausible connectivity structure on local and global dynamics in large scale brain models. J Neurosci Methods. 2009/07/18. 2009;183(1):86–94.

79. Ritter P, Villringer A. Simultaneous EEG-fMRI. Neurosci Biobehav Rev. 2006;30(6):823–38.

80. Honey CJ, Sporns O, Cammoun L, Gigandet X, Thiran JP, Meuli R, et al. Predicting human resting-state functional connectivity from structural connectivity. Proc Natl Acad Sci U S A. 2009/02/04. 2009;106(6):2035–40.

81. Deco G, Senden M, Jirsa V. How anatomy shapes dynamics: a semi-analytical study of the brain at rest by a simple spin model. Front Comput Neurosci. 2012;6:68.

82. Senden M, Goebel R, Deco G. Structural connectivity allows for multi-threading during rest: the structure of the cortex leads to efficient alternation between resting state exploratory behavior and default mode processing. Neuroimage. 2012;60(4):2274–84.

83. Allen EA, Damaraju E, Plis SM, Erhardt EB, Eichele T, Calhoun VD. Tracking whole-brain connectivity dynamics in the resting state. Cereb Cortex. 2014;24(3):663–76.

84. Matzke H, Schirner M, Vollbrecht D, Rothmeier S, Llarena A, Rojas R, et al. TVB-EduPack—an interactive learning and scripting platform for the virtual brain. Front Neuroinform. 2015;9(November):1–16.

85. Poldrack RA, Feingold F, Frank MJ, Gleeson P, de Hollander G, Huys QJM, et al. The Importance of Standards for Sharing of Computational Models and Data. Comput Brain Behav. 2019;229–32.

Supporting information captions

S1 Text. Supporting information.

S1 Table. Region labels. Labels for the 68 regions, using the same order as in the connectome. lh_* and rh_* are specifying left and right hemisphere respectively.

S2 Table. SJHMR3D parameter exploration. Parameter values used for exploring the dynamics of the SJHMR3D mean-field model.

S1 Fig. Exploration of excitation/inhibition balance, noise dispersion, mean and standard deviation of population membrane excitability. Each row of scatter plots shows a different noise level. Each column depicts a different value of n (=K12/K11). In each scatter plot X, Y and Z axis are μ, K11 and σ respectively. One can see that alpha band frequency (red) is mostly likely to occur at low noise levels, σ = 0.4, and for many values of μ, K11 and n. Dark colours correspond to alpha band activity.

S2 Fig. Exploration of standard deviation of membrane excitability (σ). Each row of plots shows the timeseries of the mean field potential (MFP); On the right, the power spectral density (PSD). For σ = 0.4, the power in the alpha band is highest. Parameters form the exploration not mentioned here are the ones used in the alpha set.

S3 Fig. Exploration of excitatory to excitatory coupling (K11). Each row of plots shows the time series of the MFP. On the right, the PSD. For K11 = 4, the power in the alpha band was highest.

S4 Fig. Exploration of the mean of membrane excitability (μ). Each row of plots shows the time series of the MFP. On the right, the PSD. For μ = 2.2, the power in the alpha band was highest.

S5 Fig. Alpha band frequency can be seen for nearly all μ, and high K11 values. However, the power (indicated by color) is highest for a low μ. Lines are drawn for better identification of points.

S6 Fig. Power spectral density (PSD) estimate for different values of n. The desired alpha frequency is observed only for n = 0.4. All coupled simulations are performed with global coupling = 0.03.

S7 Fig. Impact of inhibitory to excitatory coupling strength (K12) on the coupled network. Regions were sorted by their degree in ascending order. Frequency was log-scaled to better visualize regional differences in the slow frequency band. All other parameters were set to the alpha set parameters defined in Table 1 and 2, with global coupling set to 0.032 and conduction speed to 100. For increasing coupling the global network observes different states of synchronized and unsynchronized oscillations. In the range of K12 = 4 to 6 oscillation frequency increases with degree.

S8 Fig. No significant relation between the optimal parameters and age. For the alpha (A) and delta (B) set the plots

show age against the optimal parameter of each subject. The relation of age and optimal global coupling in the alpha set was close to significant with r = 0.2659 p-value: 0.062. The other p-values were > 0.6 for all comparisons.

S9 Fig. PLS analysis to reveal the relation between age and simulated FC. From the PLS analysis only the first latent variable (LV) was found to be significant and is reported here. It uncovers inverse relation between the SC, simFC, and SC-FC metric with age. All three measures decrease with increasing age. A PLS bootstrap ratios are shown for the LV loadings. Regions above the threshold (= 2) have reliable age-related reductions in SC, FC, and SC–FC coupling. B Bar graph showing the correlation between SC and age, simFC and age, and SC–FC coupling and age, confidence intervals on each of these correlations are shown. There is a reliable relationship between each of these and age. C Scatterplots visualizing the correlations between SC brain scores and age, simFC brain scores and age, and SC–FC brain scores and age.

S1 Video. Mechanisms of bimodality in the alpha range. Each row shows signals of a single simulation with one global coupling value G. Global coupling G was varied from top to the bottom row with values of [0, 0.025, 0.0328, 0.04]. Conduction speed was set to 100 and the other parameters were as in the alpha set. Note: In the video "xi","eta","tau" and "alpha" correspond to state variables x, y, z and w of our local model.

S2 Video. Functional connectivity and functional connectivity dynamics in dependence of global coupling. For subject #2 we show empirical FCD and FC in the left column. The right column animates how simulated FCD and FC change in relation to global coupling. The shift of global coupling is highlighted by the black vertical line in the lowest plot. In the range of ~0.029 the simulation achieves a good fit according to all three metrics, i.e. bimodality, FCD and FC comparison.

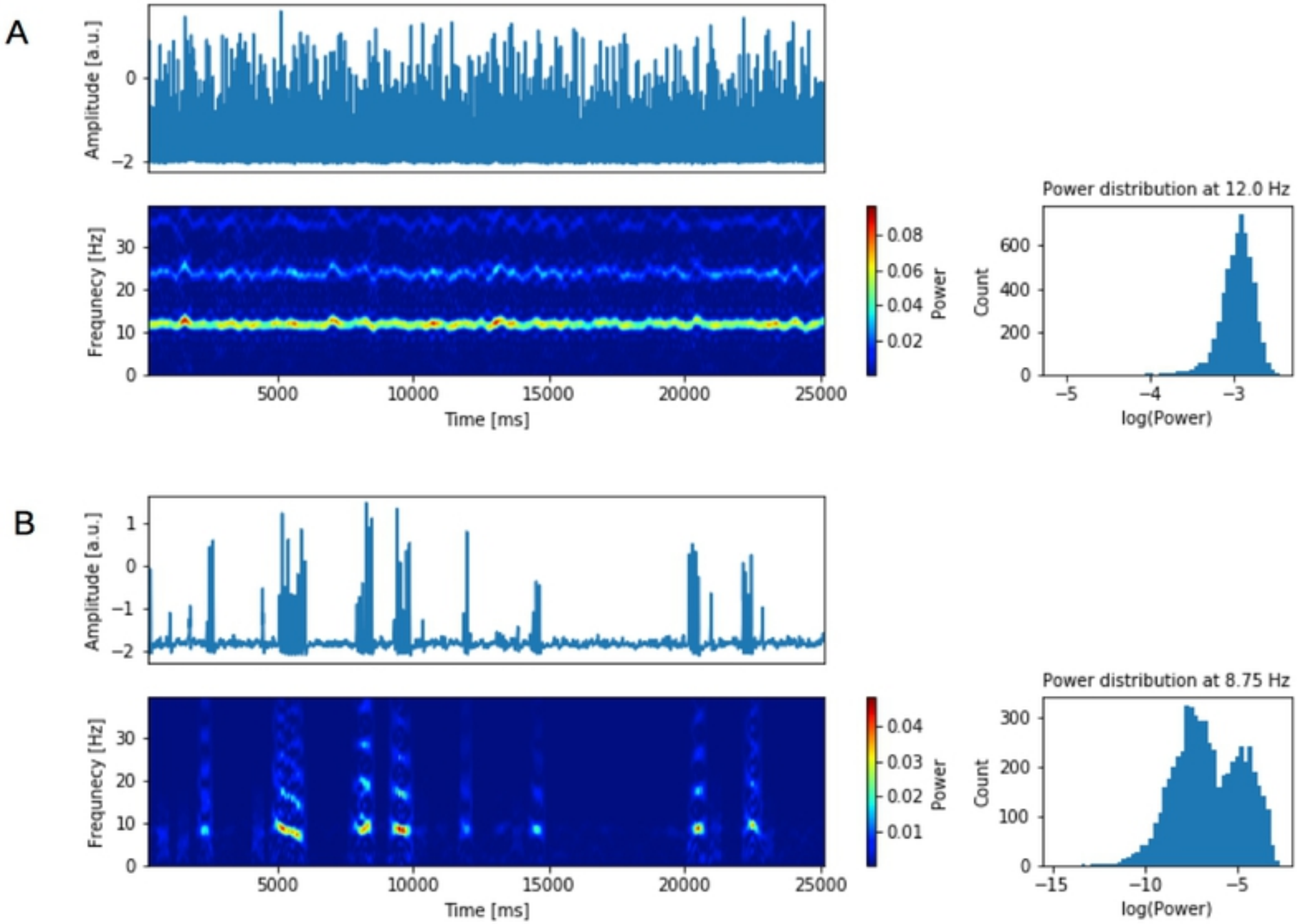
A
Amplitude [a.u.]
0
−2
Frequnecy [Hz]
30
20
10
0
5000
10000
15000
20000
25000
Time [ms]
0.08
0.06
0.04
0.02
Power
Power distribution at 12.0 Hz
Count
600
400
200
0
−5
−4
−3
log(Power)
B
Amplitude [a.u.]
1
0
−1
−2
Frequnecy [Hz]
30
20
10
0
5000
10000
15000
20000
25000
Time [ms]
0.04
0.03
0.02
0.01
Power
Power distribution at 8.75 Hz
Count
300
200
100
0
−15
−10
−5
log(Power)

Figure 1

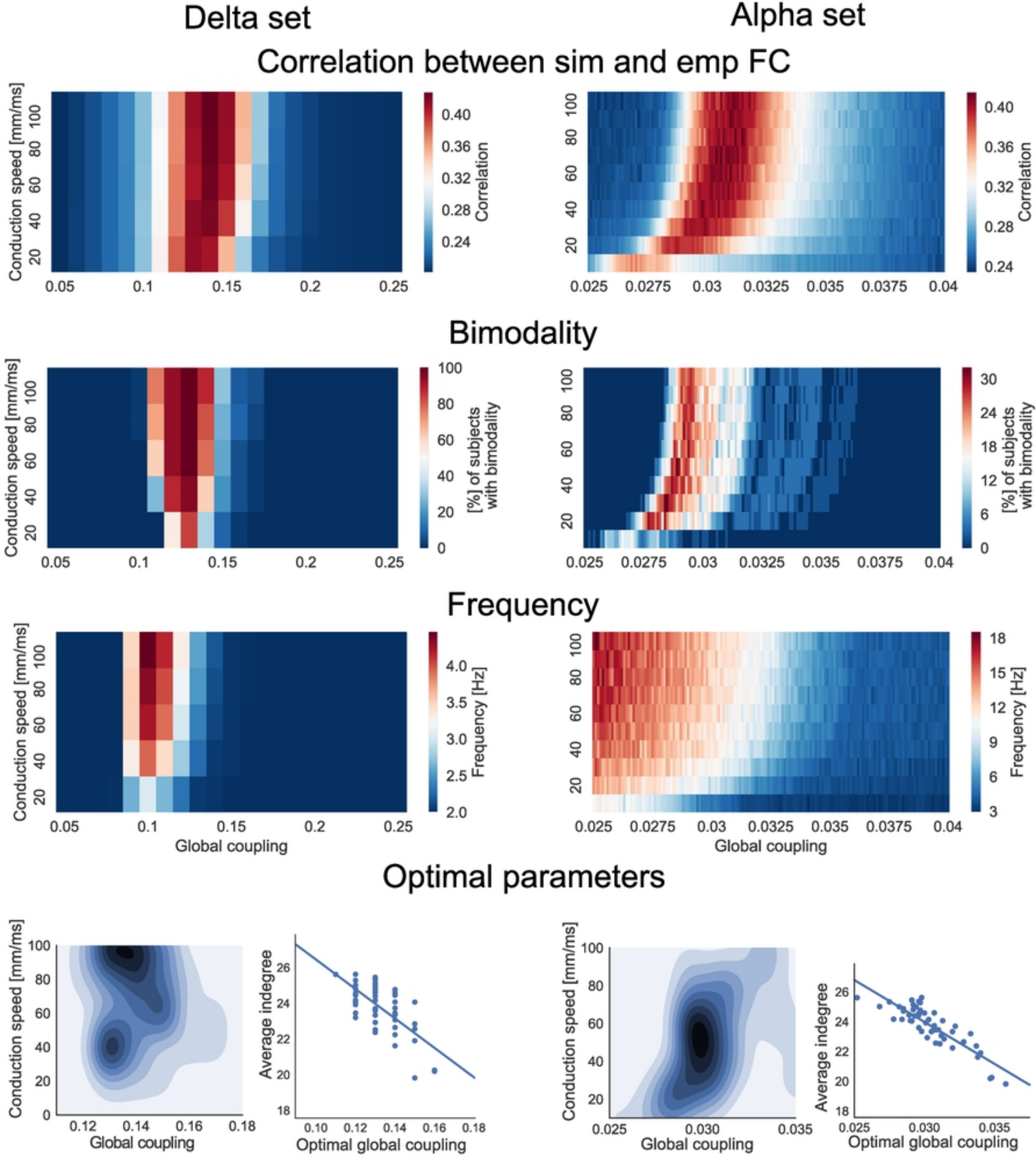
Delta set
Alpha set
Correlation between sim and emp FC
Conduction speed [mm/ms]
Correlation
Bimodality
[%] of subjects with bimodality
Frequency
Frequency [Hz]
Global coupling
Optimal parameters
Average indegree
Optimal global coupling

Figure 2

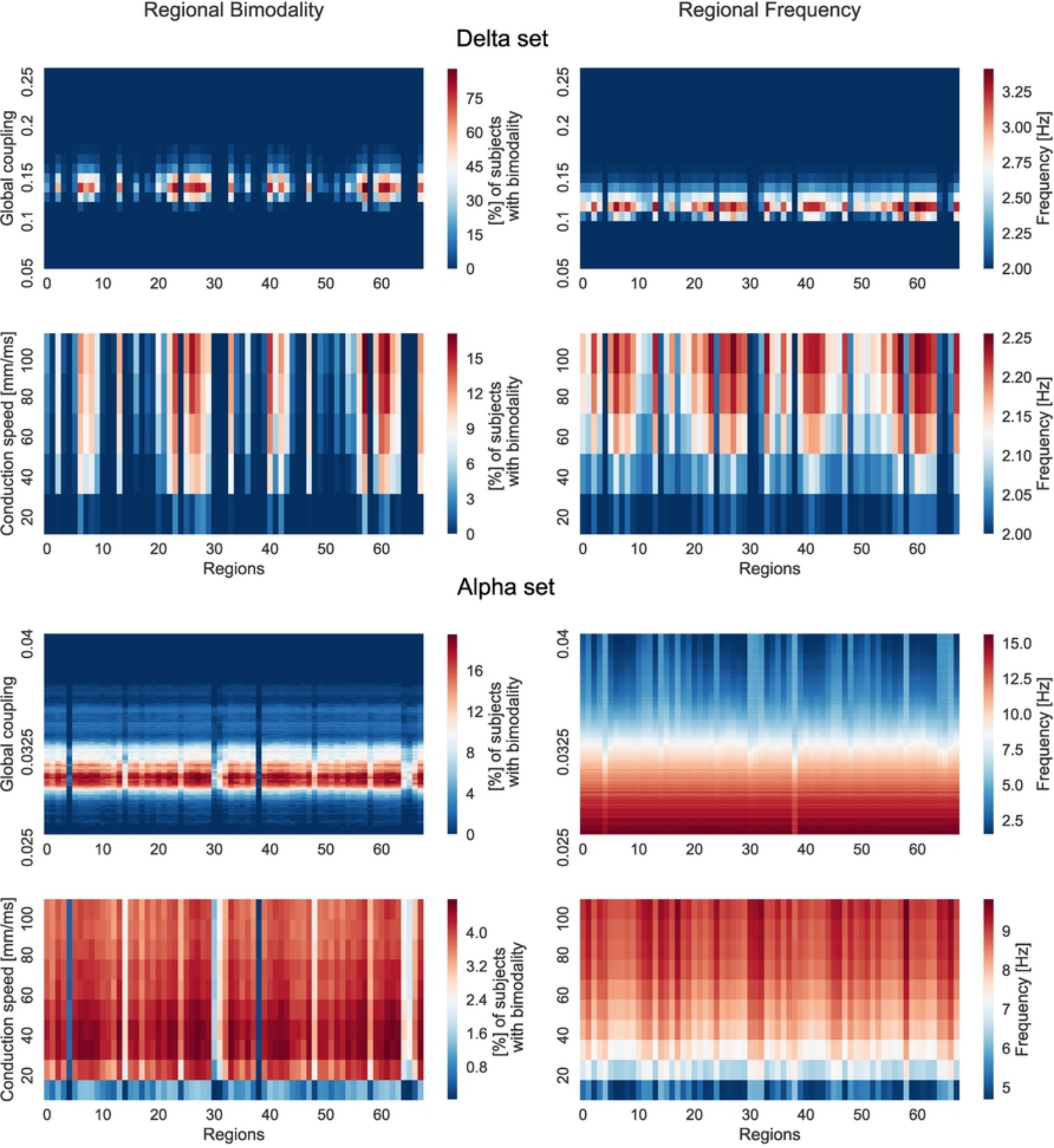
Regional Bimodality
Regional Frequency
Delta set
Alpha set
Global coupling
Conduction speed [mm/ms]
Regions
[%] of subjects with bimodality
Frequency [Hz]

Figure 3

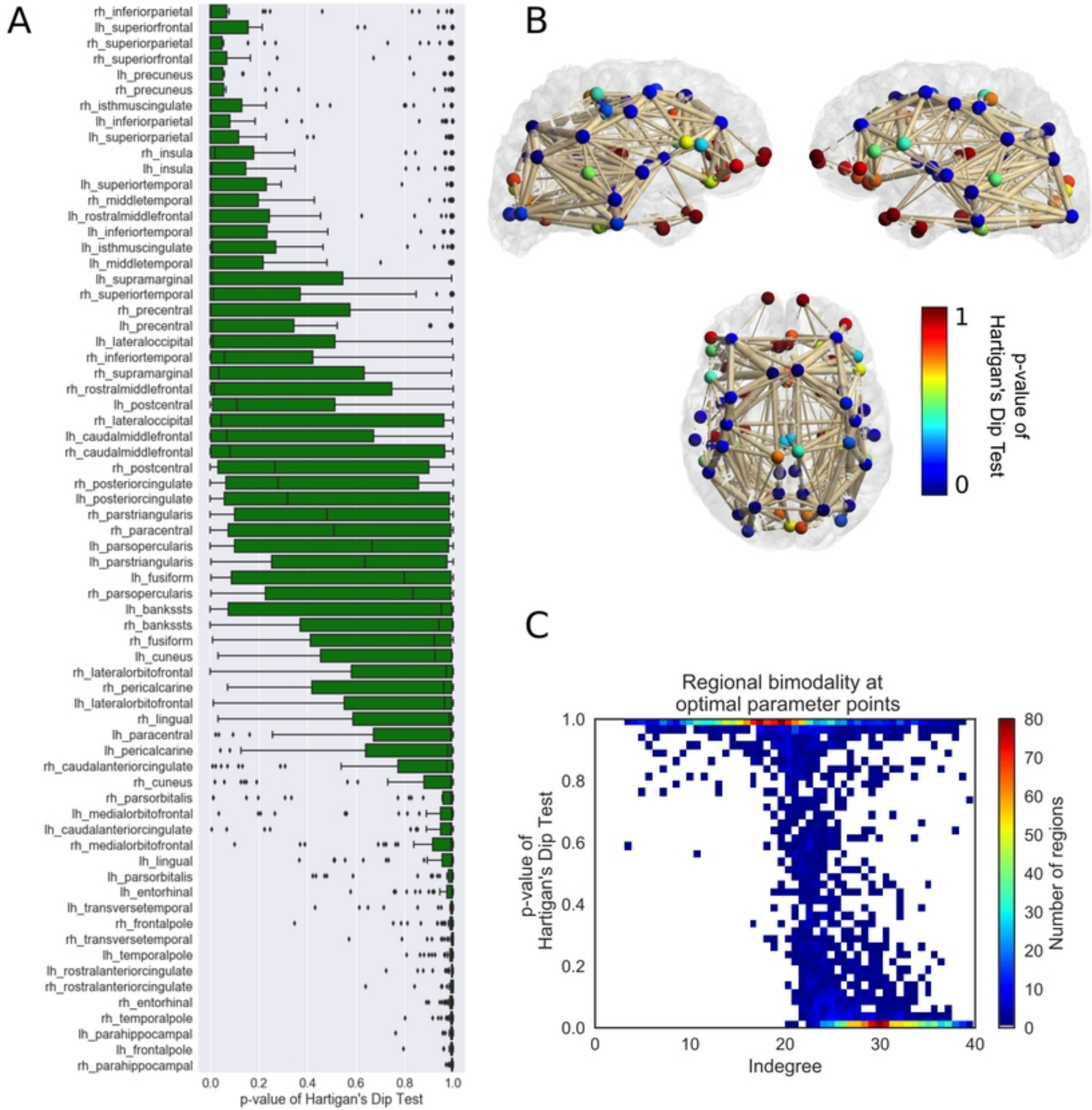
A
rh_inferiorparietal
lh_superiorfrontal
rh_superiorparietal
rh_superiorfrontal
lh_precuneus
rh_precuneus
rh_isthmuscingulate
lh_inferiorparietal
lh_superiorparietal
rh_insula
lh_insula
lh_superiortemporal
rh_middletemporal
lh_rostralmiddlefrontal
lh_inferiortemporal
lh_isthmuscingulate
lh_middletemporal
lh_supramarginal
rh_superiortemporal
rh_precentral
lh_precentral
lh_lateraloccipital
rh_inferiortemporal
rh_supramarginal
rh_rostralmiddlefrontal
lh_postcentral
rh_lateraloccipital
lh_caudalmiddlefrontal
rh_caudalmiddlefrontal
rh_postcentral
rh_posteriorcingulate
lh_posteriorcingulate
rh_parstriangularis
rh_paracentral
lh_parsopercularis
lh_parstriangularis
lh_fusiform
rh_parsopercularis
lh_bankssts
rh_bankssts
rh_fusiform
lh_cuneus
rh_lateralorbitofrontal
rh_pericalcarine
lh_lateralorbitofrontal
rh_lingual
lh_paracentral
lh_pericalcarine
rh_caudalanteriorcingulate
rh_cuneus
rh_parsorbitalis
lh_medialorbitofrontal
lh_caudalanteriorcingulate
rh_medialorbitofrontal
lh_lingual
lh_parsorbitalis
lh_entorhinal
lh_transversetemporal
rh_frontalpole
rh_transversetemporal
lh_temporalpole
lh_rostralanteriorcingulate
rh_rostralanteriorcingulate
rh_entorhinal
rh_temporalpole
lh_parahippocampal
lh_frontalpole
rh_parahippocampal
0.0
0.2
0.4
0.6
0.8
1.0
p-value of Hartigan's Dip Test
B
1
0
p-value of Hartigan's Dip Test
C
Regional bimodality at optimal parameter points
p-value of Hartigan's Dip Test
1.0
0.8
0.6
0.4
0.2
0.0
0
10
20
30
40
Indegree
80
70
60
50
40
30
20
10
0
Number of regions

Figure 4

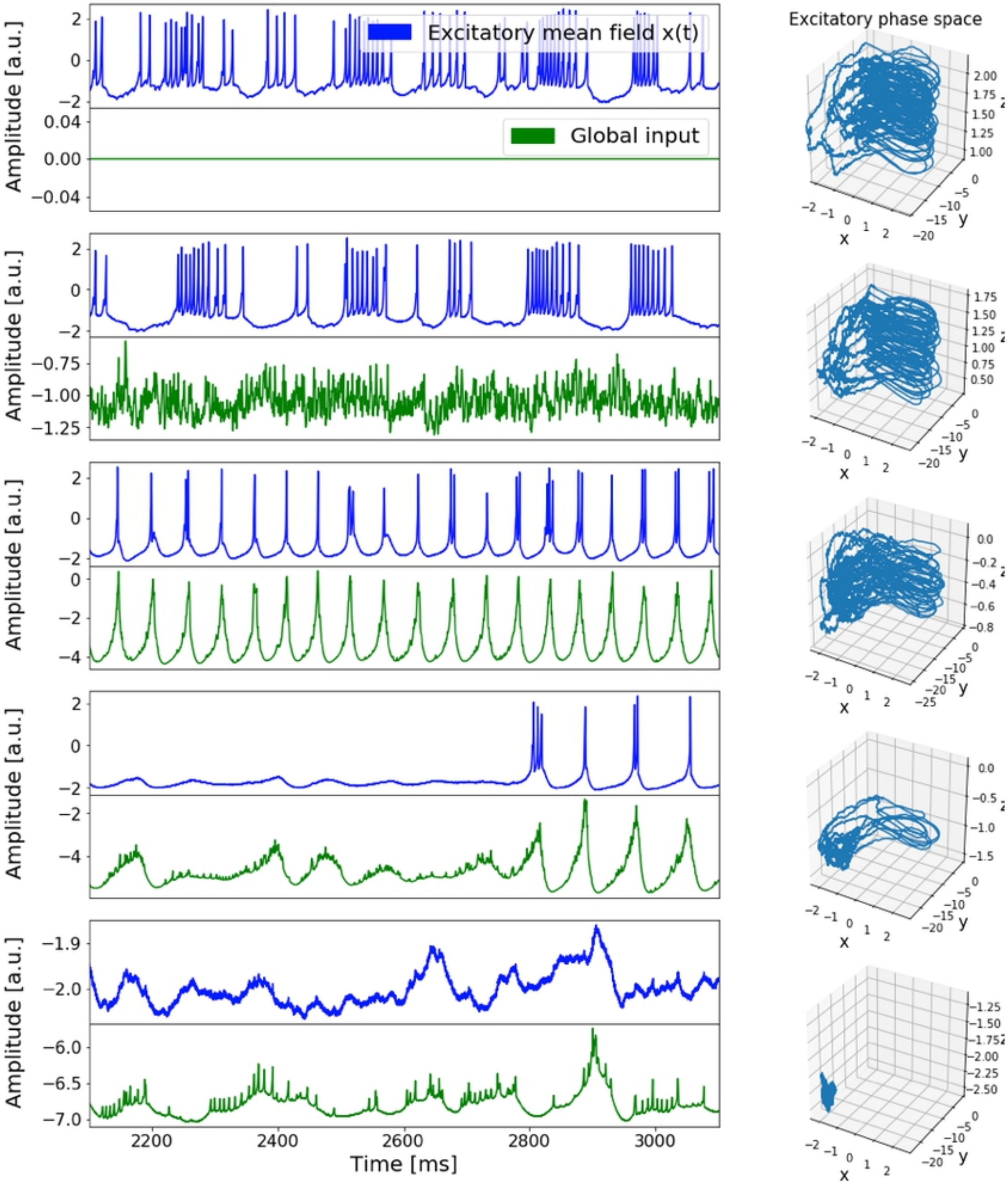
Excitatory mean field x(t)
Global input
Excitatory phase space
Amplitude [a.u.]
Time [ms]
x
y
z

Figure 5

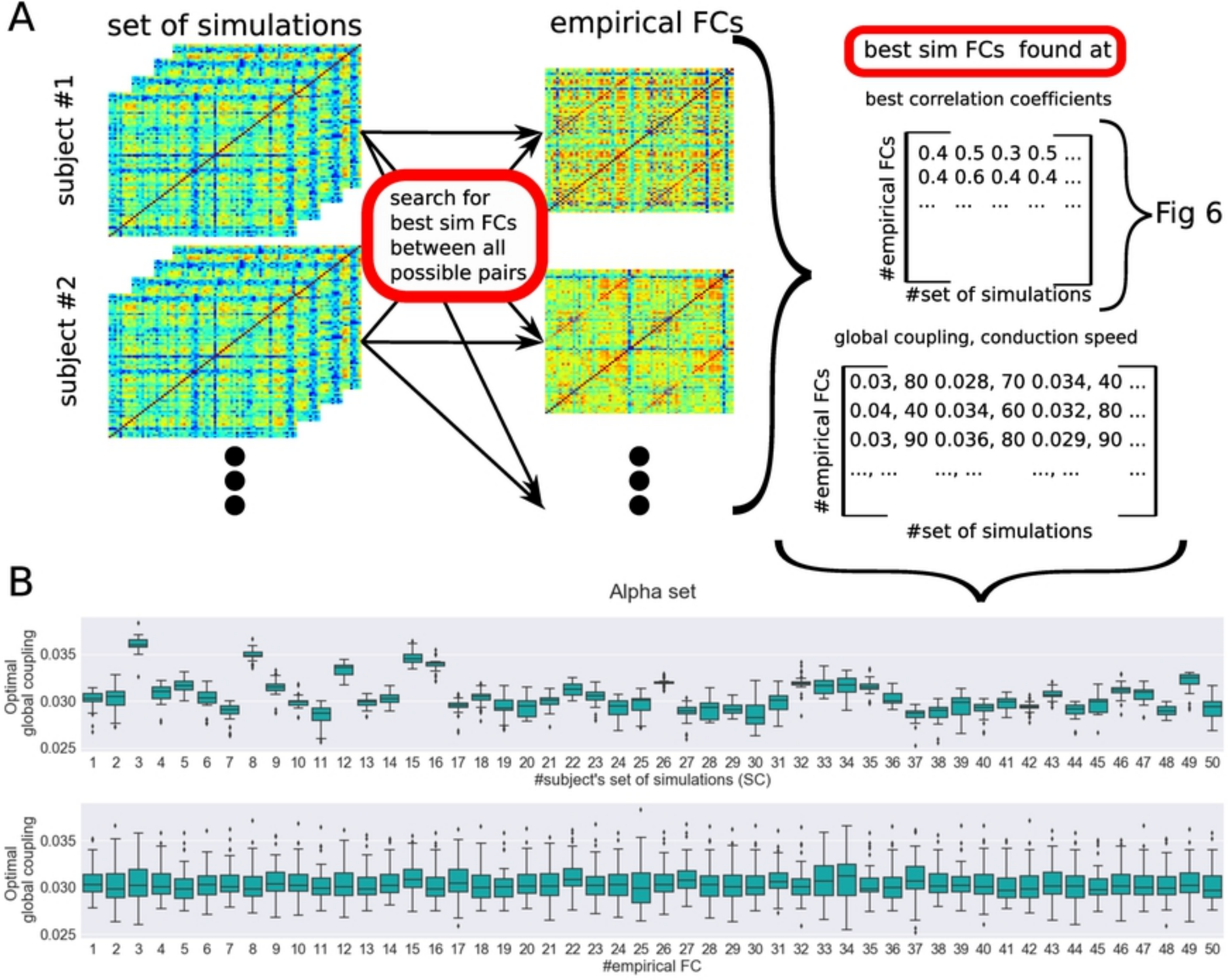
A
set of simulations
empirical FCs
subject #1
subject #2
search for best sim FCs between all possible pairs
best sim FCs found at
best correlation coefficients
#empirical FCs
0.4 0.5 0.3 0.5 ...
0.4 0.6 0.4 0.4 ...
#set of simulations
Fig 6
global coupling, conduction speed
0.03, 80 0.028, 70 0.034, 40 ...
0.04, 40 0.034, 60 0.032, 80 ...
0.03, 90 0.036, 80 0.029, 90 ...
#set of simulations
B
Alpha set
Optimal global coupling
#subject's set of simulations (SC)
#empirical FC

Figure 7

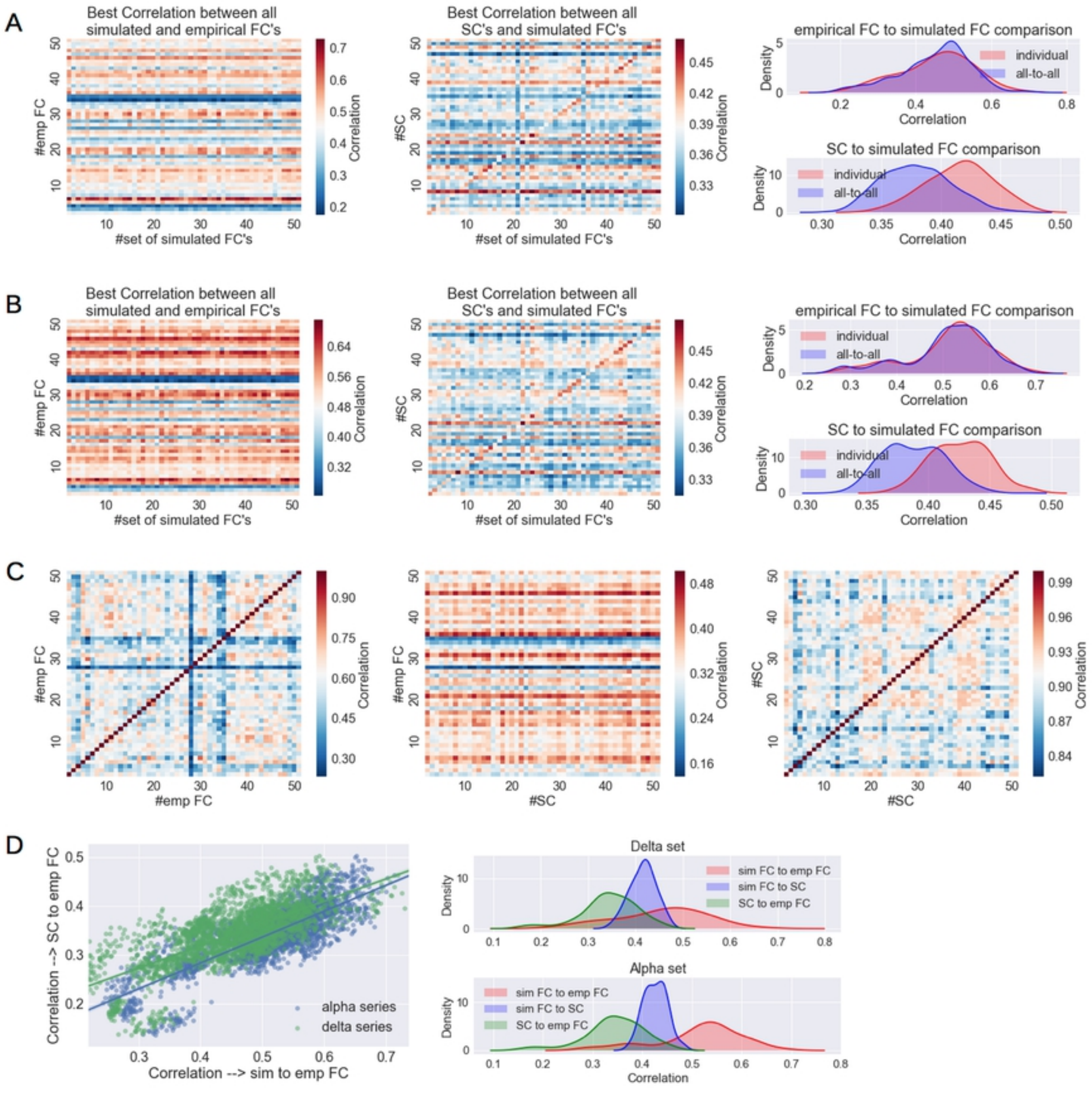
A
Best Correlation between all simulated and empirical FC's
#emp FC
#set of simulated FC's
Correlation
Best Correlation between all SC's and simulated FC's
#SC
#set of simulated FC's
Correlation
empirical FC to simulated FC comparison
individual
all-to-all
Density
Correlation
SC to simulated FC comparison
individual
all-to-all
Density
Correlation
B
Best Correlation between all simulated and empirical FC's
#emp FC
#set of simulated FC's
Correlation
Best Correlation between all SC's and simulated FC's
#SC
#set of simulated FC's
Correlation
empirical FC to simulated FC comparison
individual
all-to-all
Density
Correlation
SC to simulated FC comparison
individual
all-to-all
Density
Correlation
C
#emp FC
#emp FC
Correlation
#emp FC
#SC
Correlation
#SC
#SC
Correlation
D
Correlation --> SC to emp FC
Correlation --> sim to emp FC
alpha series
delta series
Delta set
sim FC to emp FC
sim FC to SC
SC to emp FC
Density
Alpha set
sim FC to emp FC
sim FC to SC
SC to emp FC
Density
Correlation

Figure 6

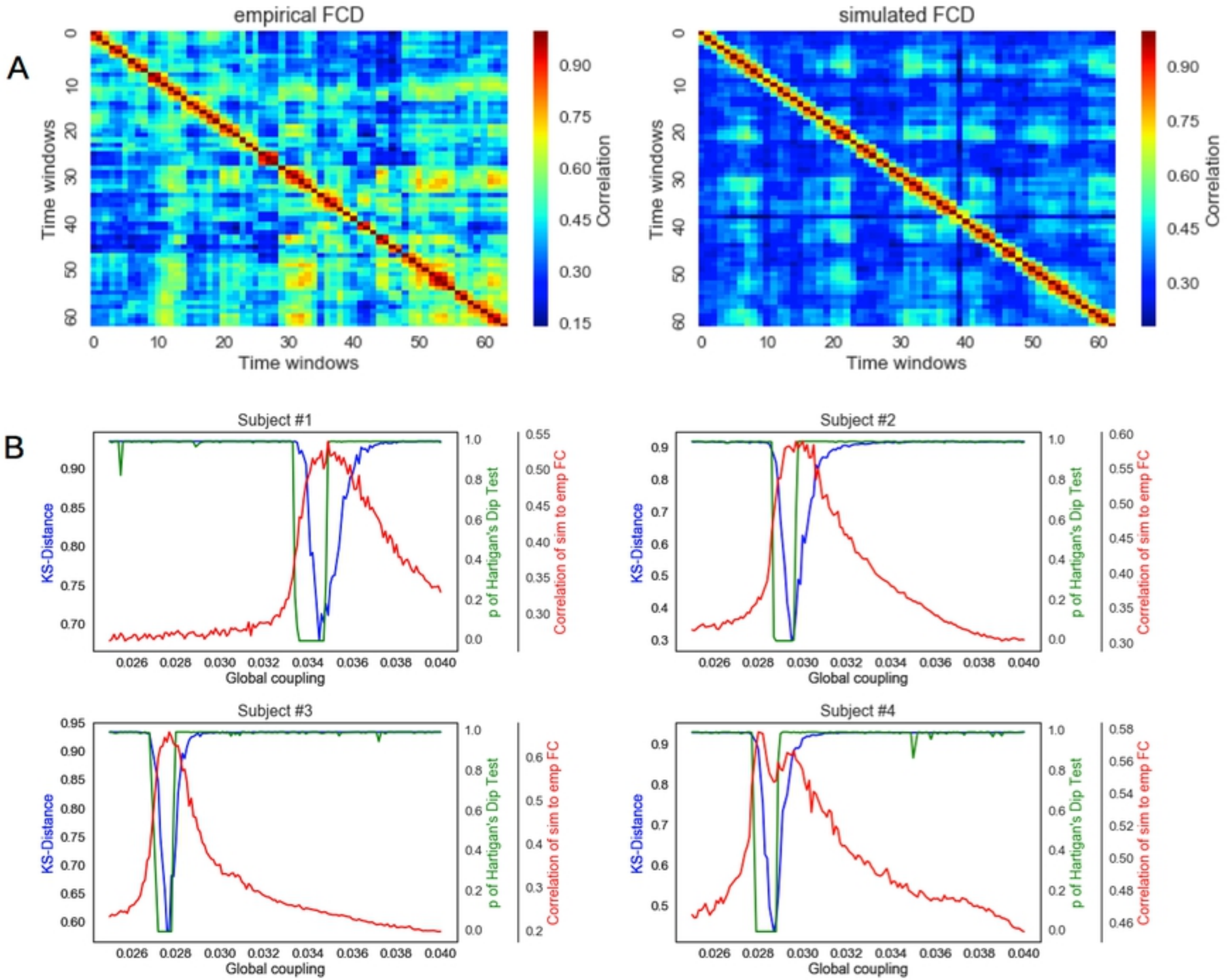
A
empirical FCD
simulated FCD
Time windows
Correlation
B
Subject #1
Subject #2
Subject #3
Subject #4
KS-Distance
p of Hartigan's Dip Test
Correlation of sim to emp FC
Global coupling

Figure 8